Johanna Unterkofler, BSc

Thermal Gradient Crystallization of Decyl-Phenyl-Benzothieno-Benzothiophene

Master's Thesis

to achieve the university degree of

Diplom-Ingenieurin

Master's degree programme: Technische Physik

submitted to

Graz University of Technology

Supervisor

Ao.Univ.-Prof. Dipl.-Ing. Dr.techn. Roland Resel

Institute of Solid State Physics

Graz, September 2019

Affidavit

I declare that I have authored this thesis independently, that I have not used other than the declared sources/resources, and that I have explicitly indicated all material which has been quoted either literally or by content from the sources used. The text document uploaded to TUGRAZonline is identical to the present master's thesis.

Date	Signature

Acknowledgement

Foremost, I would like to thank my supervisor Roland Resel for his great support. Next, Yves Geerts from the University of Brussels and his whole group, who welcomed me so warmly. It was a great pleasure to stay in Brussels for one month and preparing my samples. Furthermore, I would like to thank my colleagues here in Graz. All were great support and thanks for the fun time in the office. A special thanks to Sebastian Hofer who helped me with my heating experiments and some other measurements. Last but not least I would like to thank my family for supporting me the whole time. Thank you so much.

Abstract

2-decyl-7-phenyl-[1] benzothieno[3,2-b][1] benzothiophene (Ph-BTBT-10) gained interest, because it is an organic semiconductor and shows high charge carrier mobilities in organic thin film field-effect transistors. In this thesis, drop-casted thin films of Ph-BTBT-10 were treated with the thermal gradient crystallization technique. The thermal gradient crystallization technique is a method to perform crystallization from the melt. The samples pass through a gradient that is formed by two heating stages that are separated by a small gap, where one stage is held at a temperature above the melting point and the other stage beneath the crystallization temperature. During movement through the gradient the films were investigated with a polarized optical microscope. The phase transition from smectic A to smectic E and the final crystal phase was observed. The produced films were characterized by specular X-ray diffraction and grazing incidence X-ray diffraction. The peak positions of the specular X-ray diffraction patterns match the bulk phase peaks perfectly and are assigned to the 00l planes. So there is a preferred out-of-plane orientation with a molecular arrangement of two upright standing molecules on top of each other. However, the patterns show alternating peak widths. The odd 00l peaks are broad and the even 00l peaks are narrow. By temperature dependend X-ray diffraction measurements the peak series change to a common peak width before the phase transition. The peaks of both series melt at the expected same temperature. These observations confirm the presence of a single phase. Williamson-Hall plots were created to obtain the average crystallite size and the micro-strain. Different crystallite sizes for the broad and narrow peak series are obtained. The broad peaks result

from crystallites of an average size ranging from 30 nm to 100 nm and the sharp peaks from larger crystallites of an average size ranging from 130 nm to 770 nm. The micro-strain is inversely to the crystallite size; the smaller crystallites have larger micro-strain. The behavior of exhibiting alternating peak widths is suggested to arise from diffuse scattering due to molecular disorder.

Kurzfassung

2-decyl-7-phenyl-[1] benzothieno[3,2-b][1] benzothiophene (Ph-BTBT-10) gewann an Interesse, weil es ein organischer Halbleiter ist und hohe Ladungsträgermobilität in organischen Dünnschichttransistoren aufweist. In dieser Arbeit wurden Ph-BTBT-10 dropgecastete Dünnschichten mit der Temperaturgradienten Technik behandelt. Die Temperaturgradientenkristallisationsmethode ist eine Methode bei der Kristallisation aus der Schmelze durchgeführt wird. Die Proben durchlaufen hierbei einen Temperaturgradienten, der durch zwei Heizplatten eingestellt wird. Diese beiden Heizplatten sind durch einen kleinen Spalt getrennt. Die Temperatur einer Heizplatte ist über der Schmelztemperatur und die zweite unter der Kristallisationstemperatur des Materials. Während des Durchlaufens des Temperaturgradienten, werden die Proben mit einem polarisierten Mikroskop untersucht. Hierbei wurde der Phasenübergang zwischen Smectic A und Smectic E und die finale Kristallphase beobachtet. Die so hergestellten Filme wurden mit Röntgendiffraktometrie und mit Röntgendiffraktometrie bei streifendem Einfall charakterisiert. Die Peakpositionen der spekularen Röntgendiffraktometriemessung stimmen mit den berechneten Peaks der Bulk Phase perfekt überein und werden den 00l Ebenen zugeordnet. Daraus lässt sich schließen, dass eine bevorzugte Orientierung der Moleküle vorhanden ist. Die Wiederholeinheit sind zwei aufrecht aufeinander stehende Moleküle. Die Diffraktogramme zeigen eine Serie von Peaks mit abwechselnden Peakbreiten. Die Peaks mit ungeradem l sind breit und die Peaks mit geradem l sind schmal. Durch Röntgendiffratometriemessungen während eines Heizexperiments wurde eine gemeinsame Peakbreite aller Peaks vor dem Phasenübergang

erreicht. Beide Peakserien schmelzen bei der selben erwarteten Temperatur. Diese Beobachtungen bestätigen, dass nur eine Phase vorhanden ist. Williamson-Hall Graphen sind erstellt worden, um die durchschnittliche Kristallitgröße und die Microspannung zu ermitteln. Es wurden jeweils zwei unterschiedliche Kristallitgrößen für die geraden und ungeraden l erhalten. Den breiten Peaks liegen Kristallite von einer Größe von 30 nm bis 100 nm zu Grunde und den schmalen Peaks größere Kristallite mit einer Größe von 130 nm bis 770 nm. Die Microspannung ist invers zur Kristallitgröße. Kleinere Kristallite weisen eine größere Microspannung als größere Kristallite auf. Ein erster Eklärungsversuch der abwechselnden Peakbreiten ist, dass diese von diffuser Streuung auf Grund von molekularer Unordnung entstehen.

Contents

1 Fundamentals

1.1 Ph-BTBT-10

The reason why conjugated molecules gained interest was their potential for low cost, flexible electronics, fabrication without intense and stringent environment. These organic semiconductors can be categorized into two main classes: polymers and organic small molecules. [1]

Conductive polymers were invented in 1977 and from then on gained scientific interest. Examples for such polymers are polythiophene, polypyrrole, polyaniline. All these conductive polymers have a conjugated molecular backbone [1]. Limitations due to monomer mislinkages resulting in carrier trapping in the semiconducting channel give reason to try another class, namely organic small molecules.[2]

Molecular materials show some advantageous aspects compared to the π-conjugated polymers with aromatic and/or heteroaromatic backbones. Well-defined structure, simple purification and controllable properties due to chemical modifications of the constituent molecules are just a few of the advantages. [2]

One molecule aroused special interest because of its air-stability, namely benzothieno benzothiophene (BTBT) [2]. First symmetric side chains were added to the BTBT core, which led to a good solubility, what is crucial for the processability and higher layer crystallinity, leading to a carrier mobility higher than $10\,\mathrm{cm^2\,V^{-1}\,s^{-1}}$. [3] In the next step different substituents were added to the BTBT core that results in asymmetric

molecules [4]. For these asymmetric molecules enhanced modifiability is expected.

One of these asymmetric molecules is Ph-BTBT-10, which is used in this thesis. The molecular formula is $C_{30}H_{32}S_2$. The structure of the molecule is a benzothieno benzothiophene (BTBT) core with a phenyl (Ph) and a decyl (C10) moiety, shown in figure 1.1.

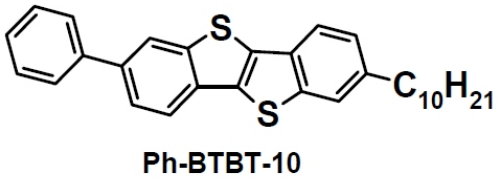

Figure 1.1: Chemical structure of Ph-BTBT-10 [3].

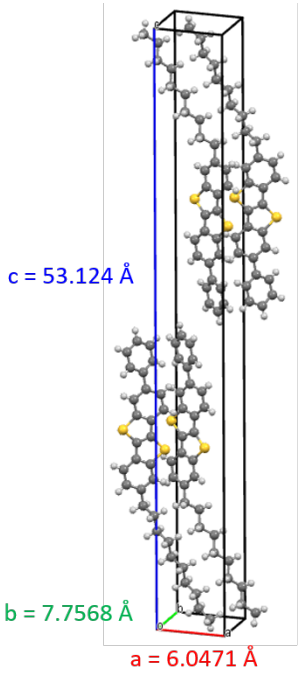

Figure 1.2: Molecular packing of Ph-BTBT-10 within the crystal structure with the unit cell parameters.

The bulk crystal structure is a head-to-head arrangement along the long unit cell axis, as can be seen in figure 1.2. There is a herringbone structure in the ab-plane that is generally present by rod-like conjugated molecules [5].

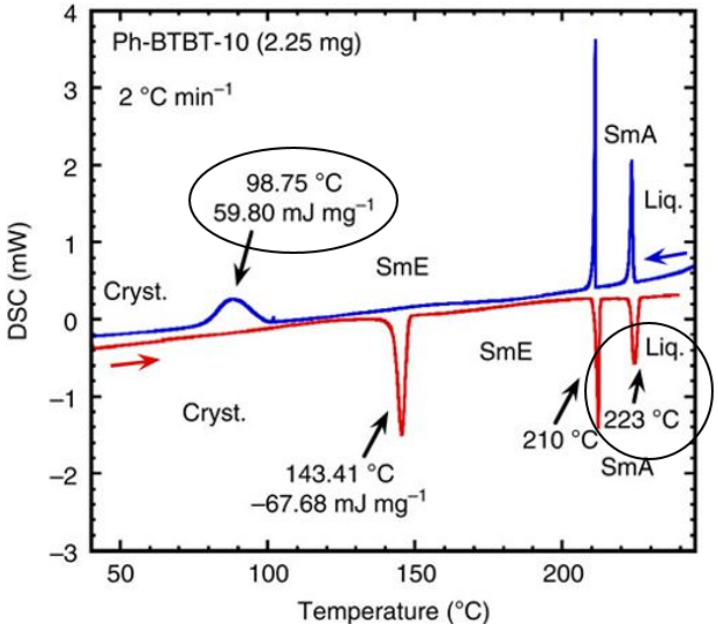

Figure 1.3: Differential scanning calorimetry of Ph-BTBT-10 [3].

In figure 1.3 the differential scanning calorimetry (DSC) of Ph-BTBT-10 is shown. The two marked temperatures are the ones important for this thesis as will be shown later. A DSC measurement gives information about the phases of a substance by measuring how much heat is required to keep both, the substance and the reference, at the same temperature. Exothermic reactions, crystallization, lead to positive signals and endothermic reactions, melting, to negative signals [6]. Heating the molecular material, it runs through different phases, indicated by the red line in figure 1.3. The phases that are present are a crystal phase, the structure is shown in figure 1.2, then it transfers to a smectic E phase (SmE) at around 143 °C and a smcectic A phase (SmA) at 210 °C before it

melts at 223 °C. Cooling down the molecule (blue line), the same phase transitions are exhibited. However, the SmE to crystal transition happens at a lower temperature than the crystal to SmE transition.

1.2 Crystallization from melts

Crystallization is the process where a solid crystal is formed out of a melt, solution or directly from the gas phase. [7] This chapter focuses on the crystallization from melts and does not deal with the other types at all.

The driving force for this process is the undercooling of the melt. Undercooling means that the melt gets cooled beneath the melting point and starts to nucleate when the undercooling is high enough. [8]

In the next section a closer look at the nucleation process is done.

1.2.1 Nucleation

Homogeneous nucleation

For homogeneous nucleation two work terms are important. Equation 1.1 shows these terms. The first part of the equation is the energy for creating the solid-liquid interface and the second part is the energy from the latent heat (ΔH) of the formation of the unit volume of the solid.

$$W_f = 4\pi r^2 \gamma_{SL} - \frac{4}{3}\pi r^3 |\Delta H| \frac{T_M - T}{T_M} \tag{1.1}$$

W_f...net work for creating a crystal
r...radius of the nucleus
γ_{SL}...interfacial energy between solid and liquid
T_M...melting temperature

Both contributions and the net curve are plotted in figure 1.4. The net curve in figure 1.4 has a maximum value for the work needed to form a crystal. The corresponding radius is called critical radius r^*.

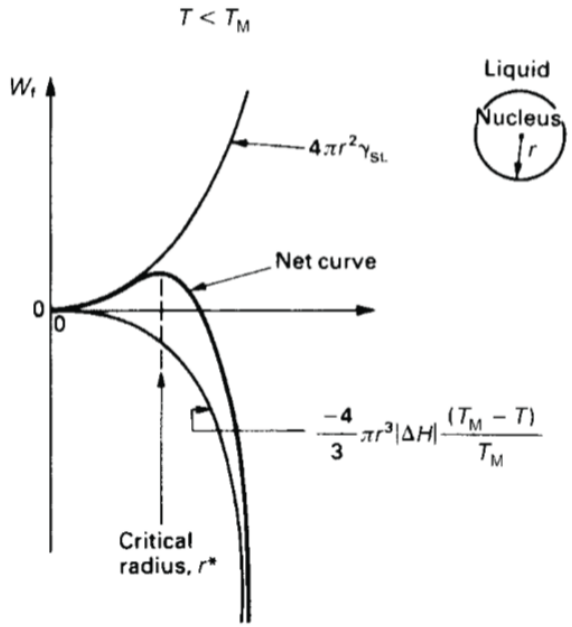

Figure 1.4: The two work terms of equation 1.1 and the resulting net work are plotted. The critical radius r^* is inserted in the graph. [8]

Randomly produced clusters with a radius below r^* are not stable and will decay. They reduce their energy by losing molecules and decreasing the radius. Nuclei bigger than r^* are stable and will continue to grow. The gain of molecules decreases the free energy. [8]

By differentiating equation 1.1 the critical radius can be calculated with the condition that $dW_f/dr = 0$ at r^*

$$\frac{dW_f}{dr} = 8\pi r\gamma_{SL} - 4\pi r^2|\Delta H|\frac{T_M - T}{T_M} \tag{1.2}$$

$$r^* = \frac{2\gamma_{SL}T_M}{|\Delta H|(T_M - T)} \tag{1.3}$$

To estimate the expected undercooling for nucleation we set $r^* = 1$ nm in equation 1.3. Using some typical values for γ_{SL}, T_M and ΔH the undercooling results in $T_m - T \approx 100K$. [8] However, nucleation starts far earlier, so the homogeneous nucleation is not the nucleation that is observed by experiments except for ultraclean laboratory samples. [8] The dominant nucleation process is the heterogeneous nucleation caused by impurities.

Heterogeneous nucleation

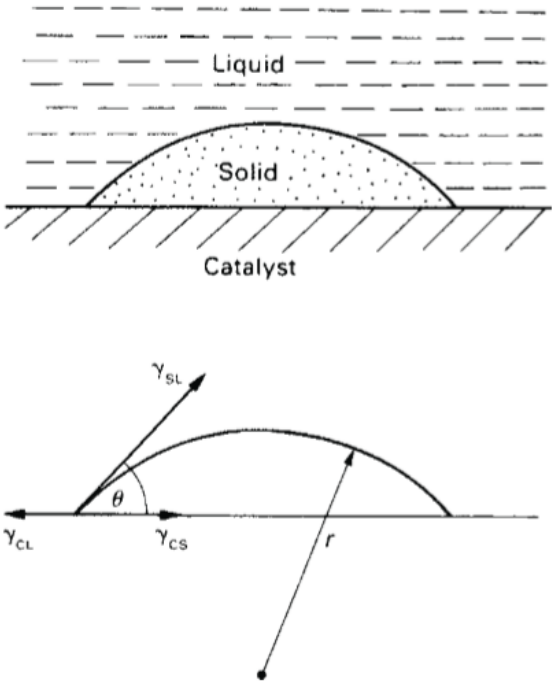

Figure 1.5: Heterogeneous nucleation. [8]

By heterogeneous nucleation the impurities in the melt act as catalysts. Assuming that the nucleus is a spherical cap sticking to the catalyst

(figure 1.5) the areas between solid & liquid and catalyst & solid can be written down as well as the volume of the spherical cap.

$$\text{solid-liquid area} = 2\pi r^2(1-\cos\theta) \tag{1.4}$$

$$\text{catalyst-solid area} = \pi r^2(1-\cos^2\theta) \tag{1.5}$$

$$\text{nucleus volume} = \frac{2\pi r^3}{3}(1-\frac{3}{2}\cos\theta+\frac{1}{2}\cos^3\theta) \tag{1.6}$$

Analogue to equation 1.1, it follows

$$\begin{aligned} W_f = {} & 2\pi r^2(1-\cos\theta)\gamma_{SL}+\pi r^2(1-\cos^2\theta)\gamma_{CS}-\pi r^2(1-\cos^2\theta)\gamma_{CL} \\ & -\frac{2\pi r^3}{3}(1-\frac{3}{2}\cos\theta+\frac{1}{2}\cos^3\theta)|\Delta H|\frac{T_M-T}{T_M}) \end{aligned} \tag{1.7}$$

γ_{CS}...interfacial energy between catalyst and solid
γ_{CL}...interfacial energy between catalyst and liquid
θ...contact angle

There are two new terms in this equation. One of the two terms corresponds to the energy that is needed to create the new interface between the catalyst and the solid, $\pi r^2(1-\cos^2\theta)\gamma_{CS}$. The other one, $-\pi r^2(1-\cos^2\theta)\gamma_{CL}$, takes into account that energy gets released due to the smaller catalyst-liquid interface after nucleation.

This equation contains too many unknowns. The triangle of forces can be used to describe the mechanical equilibrium around the edge of the nucleus.

$$\gamma_{CL} = \gamma_{CS}+\gamma_{SL}\cos\theta \tag{1.8}$$

With this relation the interfacial energy terms in equation 1.7 reduce to

$$2\pi r^2\gamma_{SL}(1-\frac{3}{2}\cos\theta+\frac{1}{2}\cos^3\theta) \tag{1.9}$$

Inserting this in equation 1.7 results in

$$W_f = \left\{1 - \frac{3}{2}\cos\theta + \frac{1}{2}\cos^3\theta\right\}\left\{2\pi r^2\gamma_{SL} - \frac{2\pi r^3}{3}|\Delta H|\frac{T_M - T}{T_M}\right\} \quad (1.10)$$

Again the same condition as before is used, $dW_f/dr = 0$ at r^* and the same relation for the critical radius results

$$r^* = \frac{2\gamma_{SL}T_M}{|\Delta H|(T_M - T)} \quad (1.11)$$

However, the two processes differ in the volume of the critical nucleus. The critical volume for the homogeneous nucleation is

$$V^*_{hom} = \frac{4}{3}\pi(r^*_{hom})^3 \quad (1.12)$$

and for the heterogeneous nucleation it is

$$V^*_{het} = \frac{2\pi}{3}(r^*_{het})^3(1 - \frac{3}{2}\cos\theta + \frac{1}{2}\cos^3\theta) \quad (1.13)$$

With the assumption that $V^*_{hom} = V^*_{het}$, the critical radius for the heterogeneous nucleation has following relation with the homogeneous critical radius

$$r^*_{het} = \frac{r^*_{hom}}{(\frac{1}{2}(1 - \frac{3}{2}\cos\theta + \frac{1}{2}\cos^3\theta)^{1/3}} \quad (1.14)$$

Arranging the particles as a spherical cap leads to a radius much bigger than arranging them as a sphere, which means that the heterogeneous nucleation dominates over the homogeneous nucleation.

1.2.2 Apparatus for crystallization

There are different ways to grow crystals out of melts. For some methods a crucible is used. However, there are also some without a crucible. The former methods can be divided into four groups. The simplest method

is that the crucible is fixed in the temperature field and the crystallization happens due to slow cooling of the crucible. Second, the crucible moves through a temperature gradient, that was done by Stockbarger and Bridgman. Also the reversed method is possible, namely that the oven is moved and the crucible is stationary. And the last one is to use a ring oven and do zone melting. For the crucible free methods, I just want to mention the Czochralski process. In this process a seed crystal of a material is put in the molten material and slowly pulled out of the melt, so that a single-crystal is the result. With this process large silicon single-crystals are produced. Seed crystals can also be used in the methods with a crucible. [9]

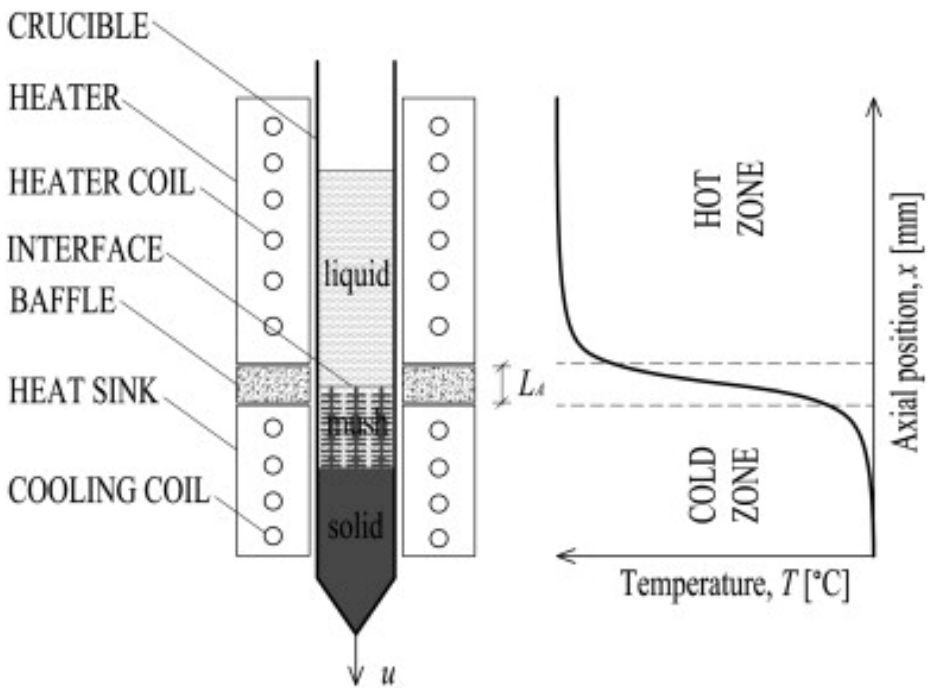

Figure 1.6: Schematic drawing of the Bridgman method and the temperature profile. [10]

The technique that is used in this thesis is based on the Bridgmann method. The Bridgman method is a method where the crystallization

takes place in a crucible that is moving through a thermal gradient [9]. The big advantage of this method is that nucleation is decoupled from the crystal growth by controlling the undercooling and the sample displacement. The motivation is to get a directional alignment of the crystal. [11]

The schematic drawing of the Bridgman method is depicted in figure 1.6 with the corresponding temperature profile.

The device used in this thesis is a horizontal version of the Bridgman method.

2 Experimental section

2.1 Drop-casting

Drop-casting is an easy and inexpensive method to prepare a film. The only requirement is that the material has to be soluble to make a solution. In this thesis, toluene is used as solvent. The used mixtures had a concentration of 8 mg/ml. $50 - 120\,\mu l$ of this solution was dropped onto a glass substrate. The used substrate is Menzel-Gläser 20×20mm #1 with a thickness of $0.13 - 0.16$mm. The glasses were cleaned with acetone, isopropanol and put in an UV/ozone cleaner, namely UV/ozone ProCleaner^{TM} Plus from BioForce Nanosciences, for at least 20 minutes.

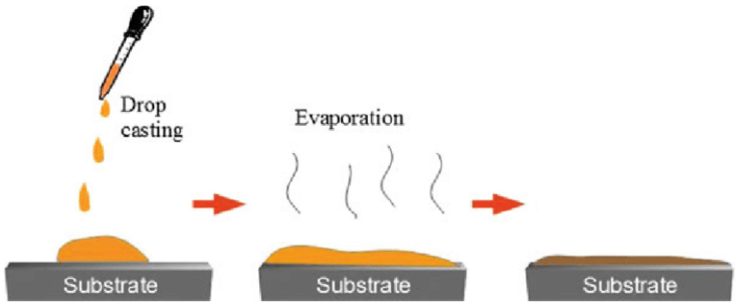

Figure 2.1: Steps of the drop-casting method. [12]

The schematic procedure of drop-casting is shown in figure 2.1. The solvent evaporates and a film of the solved compound is left on the substrate. The evaporation time is influencing the structure of the film, namely morphology and crystalline structure. [13] The evaporation took place in

ambient conditions. The molecules form islands on the substrate. A very rough film is the consequence (figure 2.2). However, the morphology of the film was not further investigated; the only aim was that the molecule is placed on the substrate. For further processing, another glass plate is placed onto the film and placed in the thermal gradient apparatus.

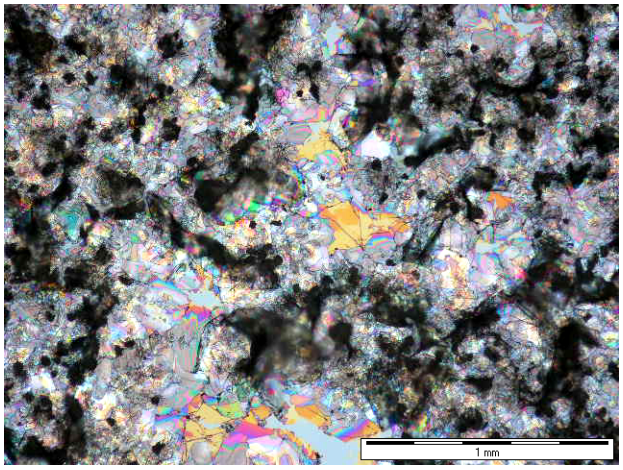

Figure 2.2: Polarized optical microscope image of a drop-casted film on a glass substrate.

2.2 Thermal gradient technique

The used thermal gradient apparatus is a Linkam GS350 temperature gradient heating stage. It consists of two independent heating stages to install the thermal gradient, figure 2.3 shows the two heating stages, the gap and the translation direction. The gap is 2.5 mm. The temperature of the hot side T_h is set to a temperature above the melting temperature of the substance and the cold side to a temperature T_c beneath the crystallization temperature. To get the desired temperatures the DSC of the compound is considered (figure 1.3). A $76 \times 26 \times 1\,\mathrm{mm}^3$ microscope glass slide (Marienfeld Cat. No. 1000000) is fixed over the heating stages on a mechanical arm and acts as a sample holder. The translation velocity

is variable between $1\,\mu m\,s^{-1}$ and $4\,mm\,s^{-1}$. To get thermal insulation from the environment the whole system is in a hermetic closed metal container. To get an insight in the crystallization behavior, the heating stage is mounted on a polarized optical microscope (POM), so images can be taken before, during and after the thermal gradient.

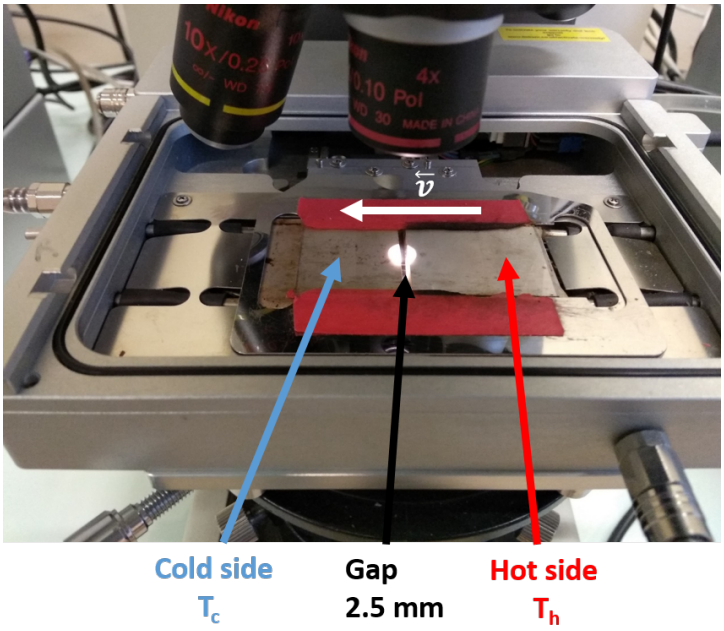

Figure 2.3: Linkam GS350 temperature gradient heating stage, T_c... temperature beneath the crystallization temperature, T_h... temperature above the melting temperature, $\vec{v}$... direction of movement, Gap... a 2.5 mm gap between the two heating stages.

The underlying principle of the thermal gradient technique is represented in figure 2.4. The graph shows the temperature over x, the gradient is installed in the gap. ΔT is the difference between T_h and T_c. T_{Melt} and T_{Cryst} are lying between these two temperatures and as soon as the sample passes the crystallization temperature, crystallization starts and can be observed with the POM.

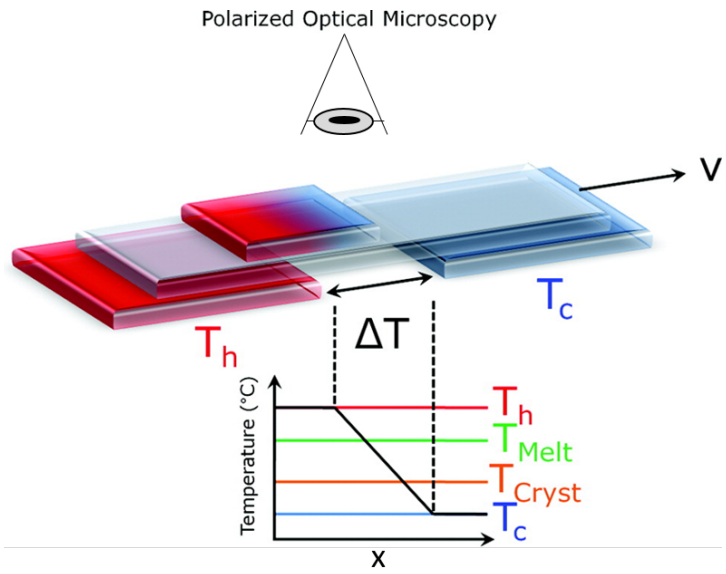

Figure 2.4: The principle sketch of the thermal gradient technique.[11]

The sandwich structure as described in section 2.1 is entirely placed on the hot stage and waited until the complete material is liquid. To check if the material is molten the polarized optical microscope is used. Under crossed polarizers the molten material appears black because the isotropic media does not change the polarization of the light, so no light gets through the analyzer, further details are in section 2.3.

The settings used for sample preparation are listed in table 2.1. There was only a small variation of the gradient possible because there was a drift in temperature even though a water cooling cycle for the cold side was installed. So, a stable gradient is achieved for T_h set to 245 °C and T_c to 75 °C. This results in the following gradient 68 °C mm^{-1}. For higher gradients T_c was not kept due to heat transfer from the hot stage to the cold stage. That is the reason why only the translation velocity could be varied and the gradient setting stayed the same. The velocity variation is between 1 and 20 µm s^{-1}. The resulting cooling rate is listed in table 2.1.

The cooling rate is:

$$C = \frac{T_h - T_c}{x} \cdot v \tag{2.1}$$

with v the velocity and x the size of the gap.

Table 2.1: List of thermal gradient samples, the selected parameters and calculated cooling rates

sample	**amount** [µl]	$\mathbf{T_h}$ [°C]	$\mathbf{T_c}$ [°C]	**v** [µm s^{-1}]	**C** [°C min^{-1}]
Sandwich1	65	240	65	10	42
Sandwich2	100	250	75	20	84
Sandwich3	65	245	75	2.5	10.2
Sandwich4	60	240	75	8	31.7
Sandwich5	60	245	75	2	8.2
Sandwich6	65	245	75	1.5	6.1
Sandwich7	50	245	65	1.5	6.5
Sandwich8	65	245	65	1.5	6.5
Sandwich9	120	245	75	4	16.3
Sandwich10	65	245	75	1.5	6.1
Sandwich11	65	245	75	3	12.2
Sandwich12	65	245	65	2.5	10.8
Sandwich13	65	245	75	1	4.1

2.3 Polarized Optical Microscopy (POM)

Light is an electromagnetic wave consisting of an electric field $\vec{E}$ and a magnetic field $\vec{B}$. The relation between these two fields are given by the Maxwell equations. Polarized light describes light with a specific

polarization direction. The polarization is defined by the direction of the $\vec{E}$ field. Three types are distinguished linear, circular and elliptical. [14]

In a POM linearly polarized light hits the sample and light with a different polarization leaves the sample if there is a birefringent material present. The $\vec{E}$ and $\vec{B}$ field of a linearly polarized wave are sketched in figure 2.5. The direction of polarization is given by the direction of the $\vec{E}$ field. The $\vec{E}$ field is perpendicular to the $\vec{B}$ field and both are perpendicular to the propagation direction, that is called a transverse wave.

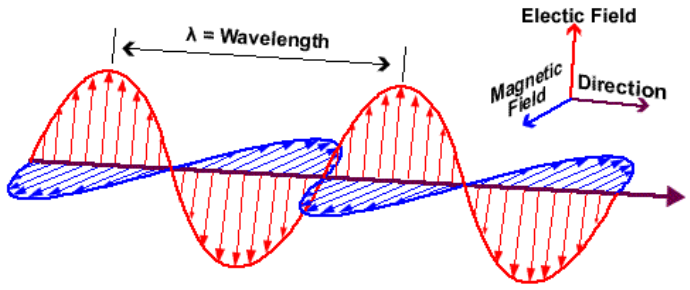

Figure 2.5: Linear polarized light. [15]

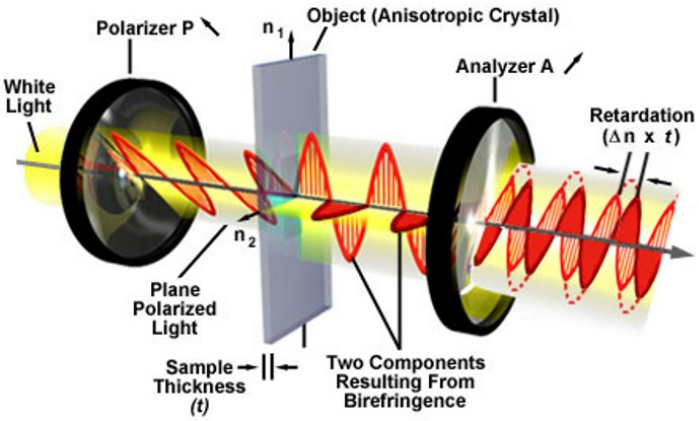

Figure 2.6: Polarized optical microscopy. [16]

Polarized optical microscopy is a good method to observe crystals and liquid crystals because anisotropic media change the polarization direction of light. Isotropic media, e.g. liquid, molten state, in contrary, do not influence the polarization and they appear black in a POM with crossed polarizers.

The schematic of a microscope is shown in figure 2.6. In POM, white light passes through a polarizer, linearly polarized light is the result. This light reaches the sample and if the sample is birefringent the light gets divided into two components and propagates through the sample with different speeds. A phase shift is the result. The phase shift describes if the outgoing wave is again linearly ($\varphi = \frac{n\lambda}{2}$), circularly ($\varphi = \frac{\lambda}{4}$ or $\frac{(2n+1)\lambda}{4}$) or elliptically ($\varphi \neq \frac{n\lambda}{4}$) polarized. [16] The analyzer, a second polarizer 90° oriented to the first one, filters the proportion of the light parallel to the analyzer direction and constructive or destructive interference happens. Not every wavelength has the same phase difference and some wavelength ranges can be cancelled out which leads to colorful images.

A Nikon Eclipse 80i polarized light microscope with the Linkam GS350 mounted on it was used.

2.4 X-Ray Fluorescence (XRF)

XRF is used to determine the atomic composition of a material. The X-rays interact with the matter and inner electrons get kicked out so the atom gets ionized (figure 2.7, photoelectric effect). An electron from an outer shell fills up the missing electron and characteristic radiation gets emitted (photon emission). Due to this characteristic lines you can identify the elements present in the material. The problem with organic molecules is that the available equipment cannot detect elements with an order number below sodium. So the sulfur in the Ph-BTBT-10 molecule and the impurities are the only measureable signals.

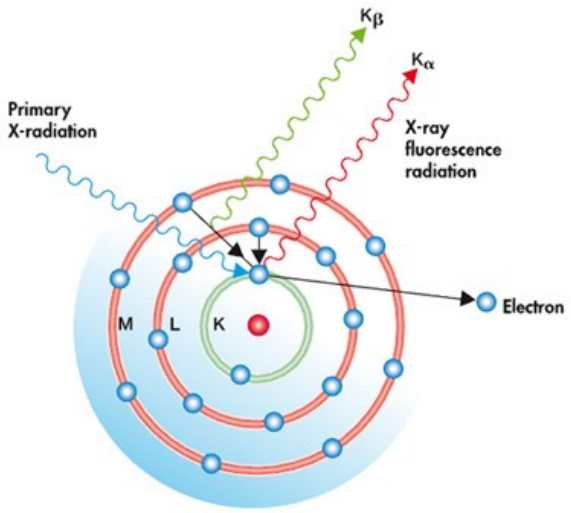

Figure 2.7: X-Ray Fluorescence principle.[17]

The used XRF device is the Epsilon 1 from Malvern Panalytical.

2.5 X-Ray Diffraction (XRD)

X-Ray diffraction is the method to characterize crystalline materials. The underlying principle is elastic scattering, which means that the diffracted wave has the same wavelength as the incident wave. This happens when x-rays interact with the electrons in the crystal. The electrons in a crystal represent the scattering centers. The theory, describing the coherent scattering by a classical free electron, was developed by J.J. Thompson, after whom it is named. It states that the electric field of the x-ray beam forces the electrons to oscillate. Consequently, the electrons emit radiation with the same wavelength as the incident wave. That is the diffracted wave and the different diffracted waves interfere constructively or destructively depending on the phase difference they have. Based on the method, x-rays provide different information of a material, including crystallinity, lattice structure, lattice defects, film thickness, roughness, crystal size,

micro-strain and macro-strain.[18]
In the following two sections the two techniques performed in this work are described.

2.5.1 Specular X-Ray Diffraction

The first method to explain is specular X-ray diffraction. This technique provides out-of-plane information which means that planes parallel to the surface are observed. In this set up the incoming beam and the diffracted beam enclose the same angle with the surface (figure 2.9, θ). A scattering vector, figure 2.8, can be defined and is the difference between the outgoing beam and the incoming beam:

$$\vec{q} = \vec{k}_{out} - \vec{k}_{in} \tag{2.2}$$

To get a Bragg peak two conditions must be fulfilled, first the length of the scattering vector $\vec{q}$ has to match the length of a reciprocal lattice vector $\vec{G}_{hkl}$ and second the scattering vector has to be perpendicular to the surface.

$$|\vec{q}| = |\vec{G}_{hkl}| \qquad \vec{q} = \vec{G}_{hkl} \parallel \vec{n} \tag{2.3}$$

The reciprocal lattice vector is:

$$\vec{G}_{hkl} = h\vec{a}^* + k\vec{b}^* + l\vec{c}^* \tag{2.4}$$

with $\vec{a}^*, \vec{b}^*, \vec{c}^*$ the reciprocal lattice vectors and hkl the linear coefficients.

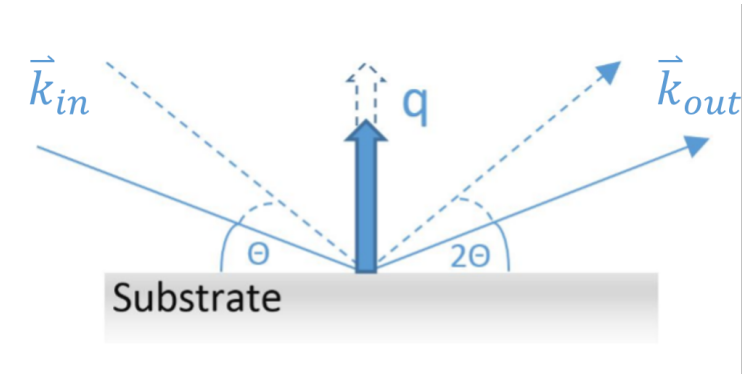

Figure 2.8: Scattering vector and the change with 2θ [19]

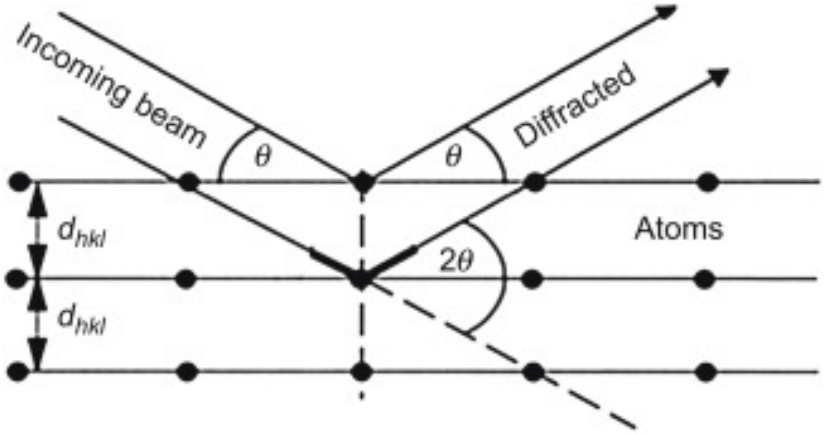

Figure 2.9: X-ray diffraction.[20]

The diffracted beams from two planes interfere constructively if they are in phase. This is the case when the path difference is an integral number of the wavelength. Mathematically described by Bragg's law 2.5.

$$n\lambda = 2d_{hkl} \cdot \sin\theta \tag{2.5}$$

With n the order of the Bragg peaks, λ the wavelength of the x-rays, d_{hkl} the distance between two hkl-planes, θ the incident angle.

XRD was performed with a PANalytical Empyrean with CuK$_\alpha$ radiation (1 in figure 2.10; x-ray tube) with a wavelength of 1.540 56 Å.

For all measurements following set up, figure 2.10, was used. On the x-ray source side the 1/32° slit (2) and a 4 or 10 mm beam mask (3) was used. A parallel beam mirror (4) and a beam attenuator (5) are also in the incident beam path. The attenuator is a 0.125 mm Ni-plate. The purpose of an attenuator is to protect the detector from too high intensity. On the detector side a 0.1 mm anti scatter-slit (6) and a 0.02 rad Soller slit (7) are mounted. The detector is a PIXcel3D detector (8). It is a solid state detector. The detector mode was set to receiving slit mode with 3 active channels. For the heating experiments a different stage (9) was mounted, namely the Domed Hot Stage (DHS) 900, explained in section 2.7.

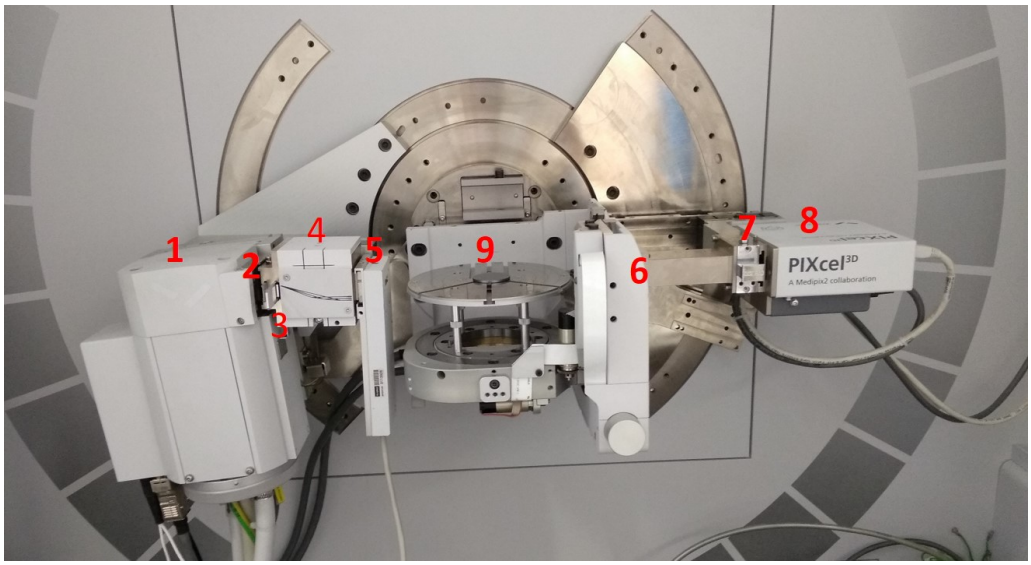

Figure 2.10: PANalytical Empyrean diffractometer with the components of the beam path marked.

2.5.2 Grazing Incidence X-Ray Diffraction (GIXD)

For grazing incidence x-ray diffraction, the incident angle is close to the critical angle of total reflection of the film. The penetration depth is limited due to this small angle. An evanescent wave emerges on the sample surface. With GIXD in-plane information is obtained. Grazing incidence X-ray diffraction is performed with synchrotron radiation due to the extremely intense and highly collimated beam.

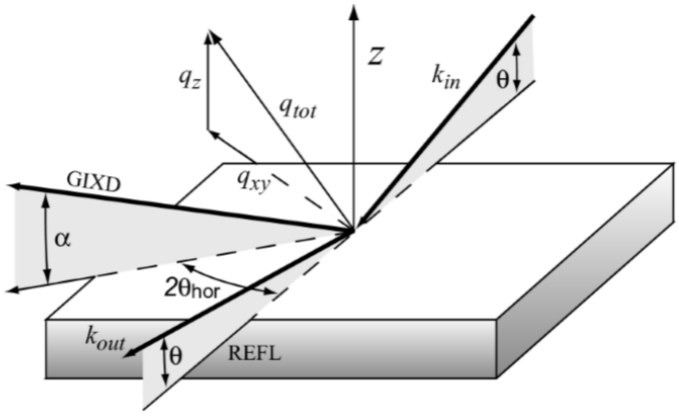

Figure 2.11: Scattering geometry for grazing incidence X-ray diffraction. θ is the incident angle. k_{in} and k_{out} represent the incoming and outgoing beams in specular direction. $2\theta_{hor}$ is the in-plane angle between the incident and diffracted beam. q_{xy} is parallel to the surface, q_z perpendicular and q_{tot} is the direction of the scattering vector. α is the angle between surface and diffracted beam. [21].

In figure 2.11 the principle of grazing incidence X-ray diffraction is depicted. For GIXD the scattering vector q_{tot} is not perpendicular to the surface anymore. q_{tot} gets splitted up into q_z ($q_\perp$, normal to the surface) and q_{xy} ($q_\parallel$, parallel to the surface) and they are: [21]

$$q_{xy} = \frac{4\pi}{\lambda} \sin\theta_{hor} \tag{2.6}$$

$$q_z = \frac{2\pi}{\lambda} \sin\alpha \tag{2.7}$$

The GIXD measurements were performed at ELLETRA on the XRD1 beamline in Trieste with a wavelength of 1.4 Å. This beamline consists of a light source that is a multipole wiggler with a range from 4 to 21 keV. The optics consist of three parts, a vertical collimating mirror, a double-crystal Si(111) monochromator and a bendable focusing mirror. The detector is a Dectis Pilatus 2M. The data evaluation was performed with the GIDVis software. [22]

2.6 Williamson-Hall method

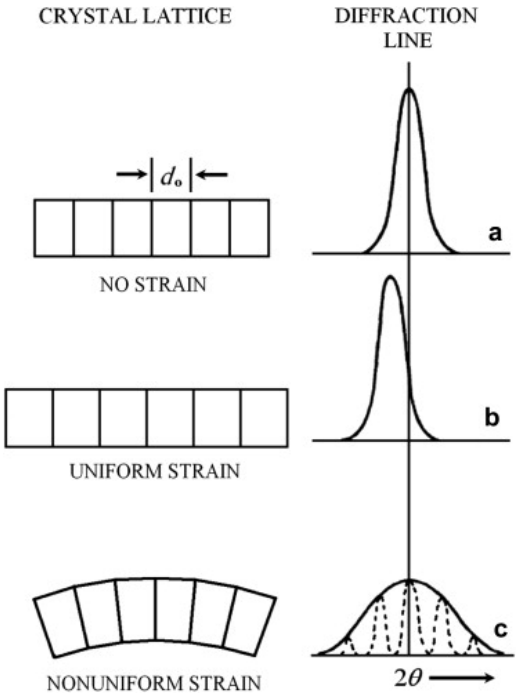

Figure 2.12: The unstrained lattice with the original peak position (a), uniformly strained lattice with a shifted peak (b), nonuniformly strained lattice with a broadened peak and less intensity (c). [23]

There are two main sources for peak broadening, first the finite crystallite size and second the inhomogeneous strain (figure 2.12) caused by lattice defects, e.g. interstitials, vacancies, dislocations and layer faults. Williamson and Hall developed a method to separate the crystallite size and the micro-strain using the peak width of an XRD pattern. The Scherrer formula (equation 2.8) relates the crystallite size L to the broadening β_L depending on θ the following way: [24]

$$\beta_L = \frac{\lambda}{L \cos\theta} \tag{2.8}$$

with λ the wavelength of the used radiation.
The peak broadening β_ε due to the micro-strain ($\frac{\Delta d}{d}$) has following dependence on θ: [23]

$$\beta_\varepsilon = 4\frac{\Delta d}{d} \tan\theta \tag{2.9}$$

Because of the quite different dependence on θ, the peak broadening β_{tot} can be written as a convolution of the micro-strain part β_ε and the crystallite size part β_L. The assumed convolution is just a sum of both effects, equation 2.10 follows.

$$\beta_{tot} = \beta_L + \beta_\varepsilon = \frac{\lambda}{L \cos\theta} + 4\frac{\Delta d}{d} \tan\theta \tag{2.10}$$

Multiplying equation 2.10 with $\cos\theta$ results in the relation 2.11:

$$\beta_{tot} \cos\theta = \frac{\lambda}{L} + 4\frac{\Delta d}{d} \sin\theta \tag{2.11}$$

Plotting $\beta_{tot} \cos\theta$ in respect to $\sin\theta$ one can extract the crystallite size from the intersection with the Y-axis and the strain from the slope of the linear fit. [25]

The problems occurring by the Williamson-Hall method are that it cannot be used for non-spherical crystallites and non-uniform micro-strains. To get a good result one should have a series of peaks from one direction, in this case 00l up to the order of l = 14.

2.7 Domed Heating Stage DHS 900 / 1100

The DHS900 can be mounted on the PANalytical Empyrean and in-situ XRD measurements can be done. [26] The stage can be heated up to 900 °C. Above 200 °C a compressed air shower turns on to cool the dome that is mounted over the sample to protect the sample from oxidation at high temperatures. The dome is flushable with nitrogen to get a protective atmosphere. The used dome is made of graphite. The DHS 900/1100 is connected with a TCU150/200 Temperature Control Unit. The temperature profile is set by the software iTools TCU150. Different heating ramps up to 300 °C min^{-1} are possible.

The DHS1100 is a next step of the DHS900. [27] A temperature up to 1100 °C can be reached. In figure 2.13 the DHS1100 is shown and the used graphite dome. With the DHS1100 the cooling experiments from section 3.3 were performed.

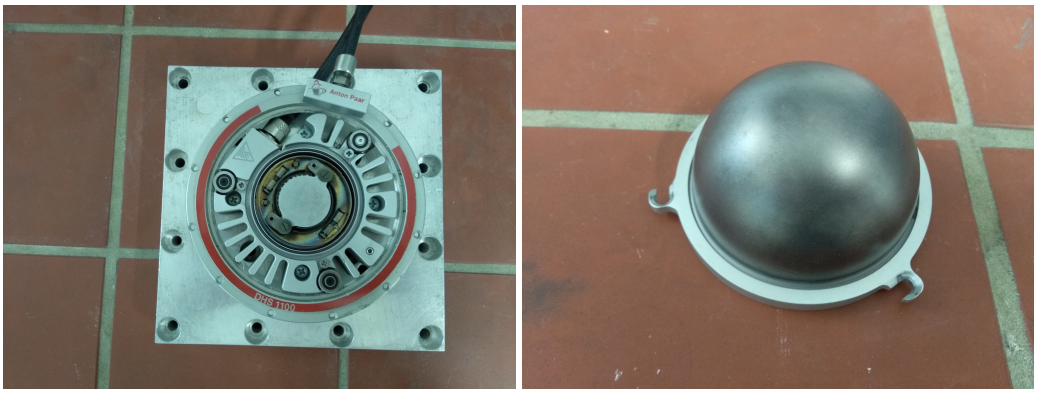

(a) DHS1100 (b) Graphite dome

Figure 2.13: The heating stage DHS1100 and the graphite dome

3 Results and Discussion

3.1 Comparison of two material sources

The used material was synthesized in Brussels, Belgium and colleagues from Graz used the same molecule but synthesized in Milano, Italy. The two material sources are compared in respect to atomic composition and phase behavior.

3.1.1 X-Ray Fluorescence (XRF)

Both materials were analyzed by XRF. The elemental composition is listed in table 3.1

Both materials show a signal of about 98% sulfur, so they are both quite clean. If the material would be perfectly clean there should be 100% sulfur because all the other elements (C,H) of the molecule are not detectable by the used XRF equipment. The impurities come from the synthesis and the used foil (Mylar Thin-Film) in the measurement set-up. The impurities assigned to this foil are Ca, P, Fe and Zn. The signal of these impurities is quite small except for Ca and P. These two also come from the synthesis that explains the higher amount. However, they have a quite small signal and the percentage number does not mean that the compound possesses for example 0.2% Si just that this percentage of the signal is corresponding to Si. The Si can come from the glas vessel the material was stored in.

Table 3.1: The XRF result of both material sources

Belgium material		Italian material	
Element	**%**	**Element**	**%**
S	98.075	S	97.879
Si	0.182	Si	0.217
P	0.520	P	0.473
Al	0.822	Al	0.815
Ca	0.364	Ca	0.569
Fe	0.015	Fe	0.020
Co	0.013	Co	0.017
Br	0.001	Br	0.002
Cr	0.007	Mn	0.005
Zn	0.002	Ni	0.003

3.1.2 Polarized Optical Microscopy (POM)

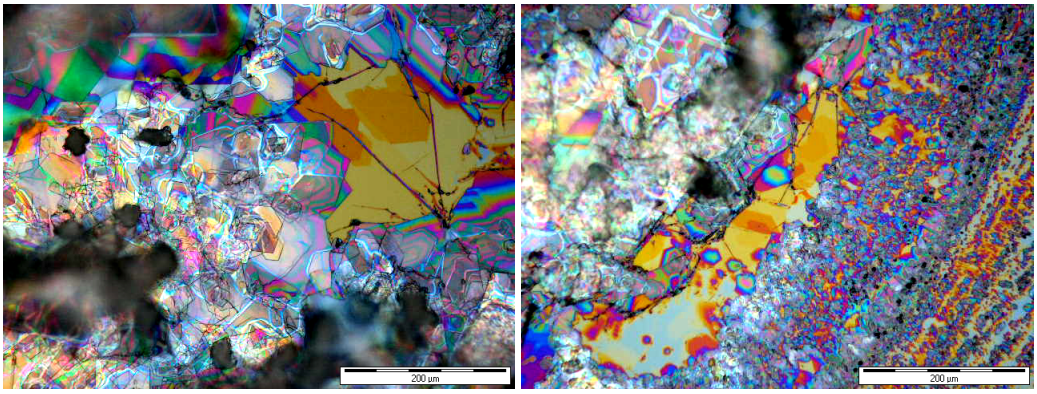

(a) (b)

Figure 3.1: POM of the drop-casted samples (a) with the Belgium material and (b) with the Italian material.

To check the crystallization behavior, both materials were used to prepare a drop-casted thin film under the same conditions, a silicon wafer was used as substrate. These samples were observed by POM and measured with XRD. The POM evaluation shows that both materials form a comparable morphology on the silicon wafer, figure 3.1. There are larger and smaller plate like crystallites forming on the substrate.

3.1.3 Specular X-ray Diffraction

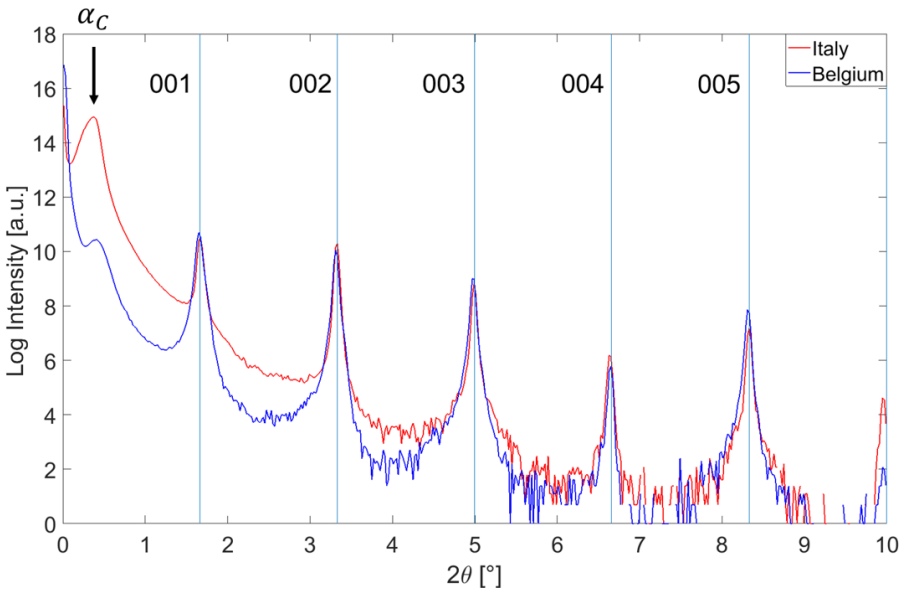

Figure 3.2: Drop-casted samples from the Belgium and Italian material. The blue vertical lines are the peak positions for the bulk crystal structure.

An XRD measurement of these drop-casted samples is shown in figure 3.2. The blue curve is the XRD pattern from the Belgium material and the red curve the pattern from the material from the Italian source. The blue vertical lines indicate the calculated Bragg peak positions of the 00l planes of the known bulk structure and fits the measured data perfectly. Apart

from the worse alignment (shape of critical angle, α_c) of the Belgium sample both materials show the same XRD pattern and from that one can conclude that the same crystal structure is present.

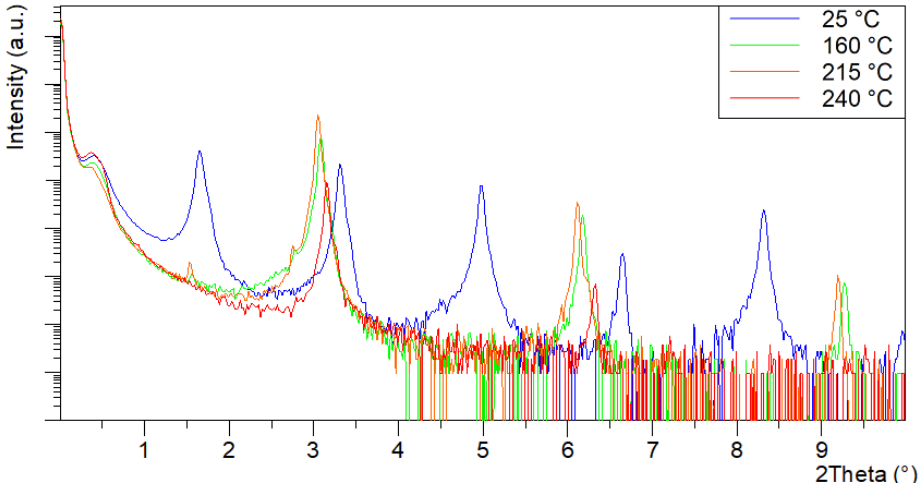

Figure 3.3: Heating of the Belgium sample from room temperature to 240 °C. In the graph there are the XRD pattern for the different phases. The blue line is the known bulk structure, the green and orange line is the pattern for the SmE phase and the red curve is the SmA phase.

In the next step the phase behavior was inspected. For the heating experiments, the heating stage DHS 900 was mounted on the Panalytical Empyrean and in situ XRD measurements were performed. Measurements at certain temperatures were taken. The temperature profile is set via the iTools TCU150 software. The two graphs, figures 3.3, 3.4, depict the measurements for the two samples at the same temperatures. The blue curve shows the normal already solved bulk crystal structure. The green curve is the SmE pattern. Although the orange curve is at a temperature assigned to the SmA phase in the DSC curve the heating experiment shows a slightly shifted SmE pattern. The red curve in the Belgium material pattern is a SmA with a peak shift closer to the bulk peaks. In the Italian pattern there is no signal so the material is already molten. This

is the expected phase because according to the DSC the liquid phase is present above 223 °C. For the Belgium material the melting process is also observable because there is no 003 peak and the two peaks observed have a quite low intensity. A possible explanation is that the heat transfer from the heating plate through the silicon wafer to the film takes some time and the waiting time was too short to get in an equilibrium state.

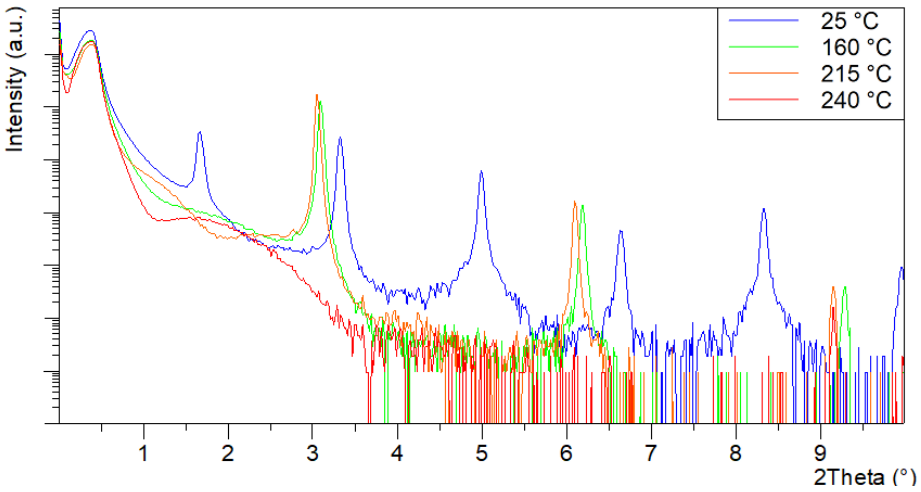

Figure 3.4: Heating of the Italian sample from room temperature to 240 °C. The blue line is the bulk phase, the green and orange line are in the SmE phase and the red one is the pattern for the liquid state, indicated by the missing Bragg peaks.

For the Belgium material the isotropic phase appeared at 250 °C. Cooling back to room temperature recrystallization happens. For the Belgium material a cooling rate of 0.25 °C min^{-1} was taken. For the Italian material the cooling rate was not set to a specific rate. The heating stage was just turned off. The resulting XRD pattern are depicted in figure 3.5. The pattern shows all Bragg peaks but with less intensity as before. Also broad and narrow peaks are alternating. This indicates that there is not a perfect crystal present but a quite disorder. Besides that, both materials are identical.

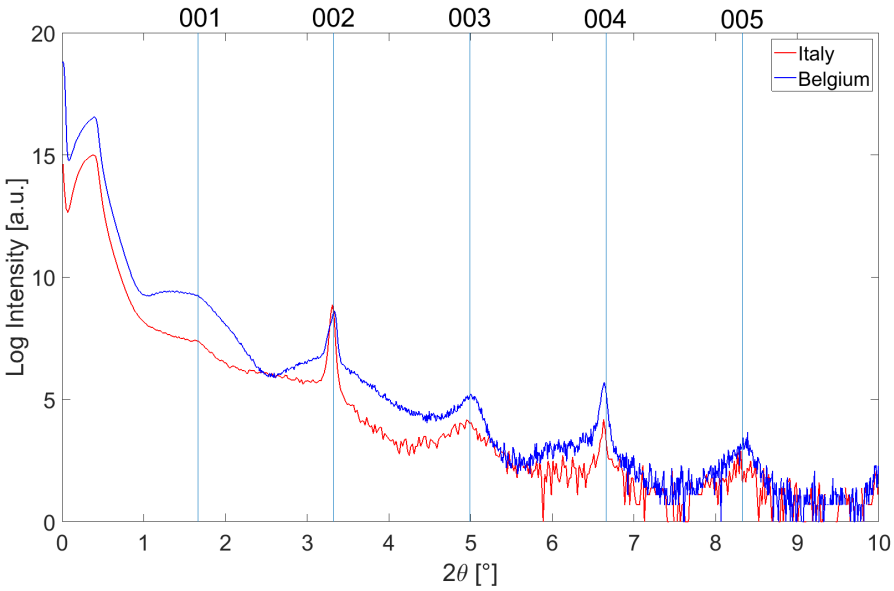

Figure 3.5: XRD of drop-casted samples from the Belgium and Italian material recrystallized form the melt with an undefined cooling rate for the Italian material and a cooling rate of 0.25 °C min^{-1} for the Belgium material. The blue vertical lines are marking the Bragg peaks of the bulk crystal structure.

3.2 Thermal gradient crystallization samples

3.2.1 Before thermal treatment

In section 2.2 the procedure of preparing the samples in a thermal gradient is explained. The samples were characterized by XRD and GIXD. For comparison of the effect of the thermal gradient an XRD measurement of the just drop casted sample was performed. The resulting pattern (figure 3.6) fits the known bulk structure very well, indicated by the blue vertical lines that are the calculated peak positions of the known bulk structure. The d-spacing is calculated with Bragg's law, equation 2.5 and is 53.08 Å that corresponds to two upright standing molecules just like in the

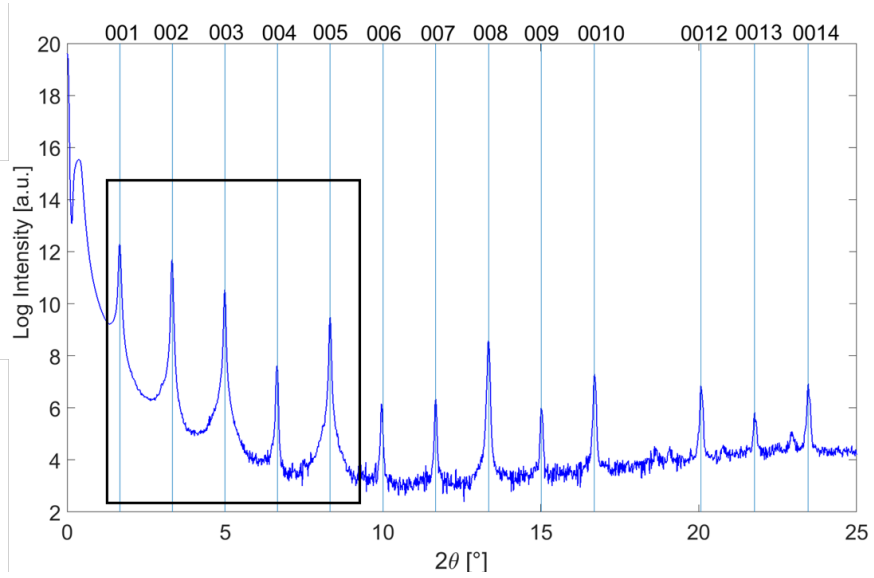

Figure 3.6: Drop-casted as prepared. The blue lines indicate the calculated peak positions for the 00l peak series. The black box marks the region that is depicted in figure 3.7.

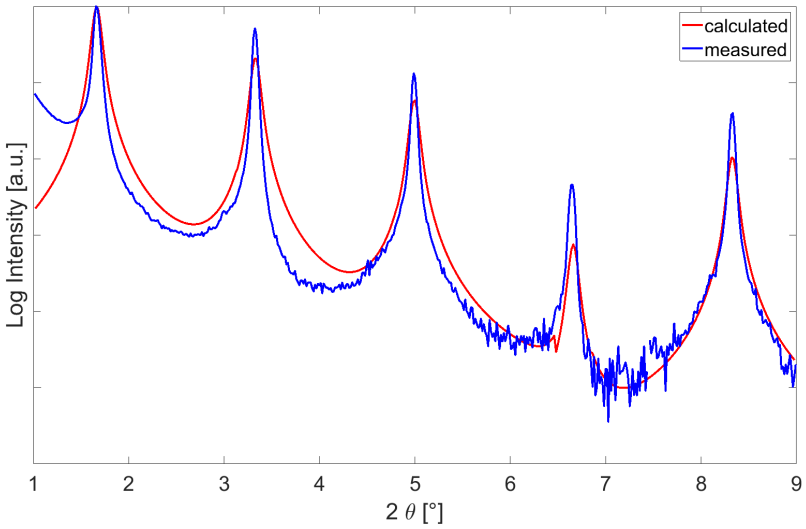

Figure 3.7: Comparison of the calculated and the measured intensity.

bulk structure (figure 1.2). Also the calculated intensities of the bulk

phase fit quite well, figure 3.7. Although, the measured intensity is a little bit higher than the calculated. Reasons for that are the settings for the calculation of the powder pattern. The full width at half maximum and the wavelength of the x-ray source are needed. There are always some deviations from the experimental set-up. The calculation was done with Mercury CSD 4.0.0.

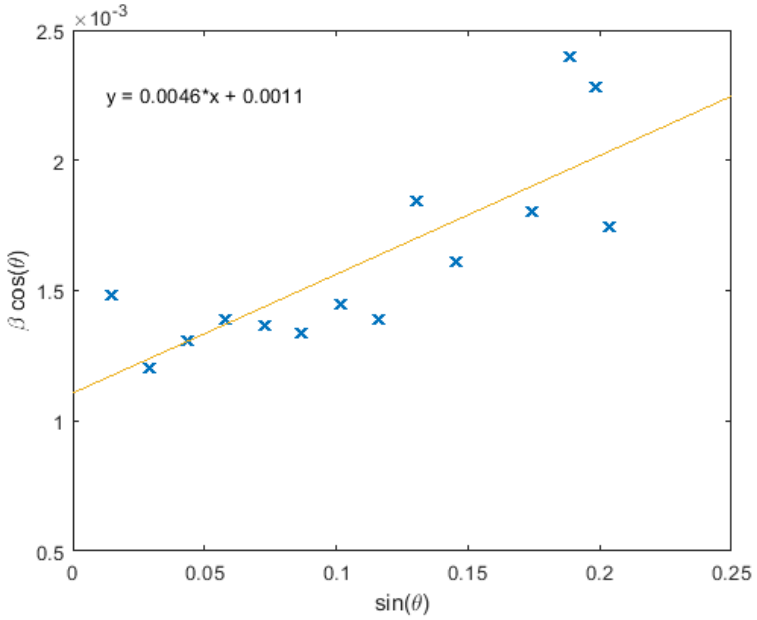

Figure 3.8: The Williamson-Hall plot of the just drop-casted sample (figure 3.6). The blue markers are data points calculated from the peak position and the integral breadth of the peak. The yellow line is the linear fit of the data points. With that, a crystallite size of 1402 Å was calculated and a micro-strain of 0.0012 (0.12%).

Because of the nice series of Bragg peaks resulting from one plane family, a Williamson Hall plot is created (figure 3.8). In the Williamson-Hall plot $\sin\theta$ is plotted in respect to $\beta\cos\theta$. β is the integral breadth of the peak and θ is half of the 2θ angle read out from figure 3.6. In the left corner of figure 3.8 the equation for the linear fit is added. With this equation, the crystallite size and the micro-strain were calculated. This led to a

crystallite size of 1402 Å and a micro-strain of 0.0012 (0.12%). As can be seen all the peaks are nicely fitting the predicted linear behavior.

3.2.2 After thermal treatment

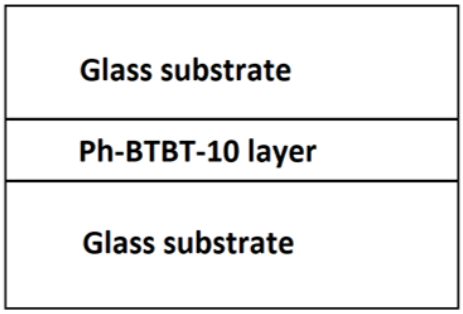

Figure 3.9: Thermal gradient sample structure, Ph-BTBT-10 layer sandwiched between two glass plates.

In the next step the drop-casted samples were treated with the thermal gradient technique. The described sandwich structure is shown in figure 3.9. During the gradient they were investigated by POM. Figure 3.10 shows a sample translating through the gradient. The direction of the movement is indicated by the arrow below the image. The white line shows the transition front. On the right side the SmA phase can be observed and on the left side the SmE phase is present. These two phases are identifiable through the focal conic fan texture and the additional arcs across the fans in the SmE phase. [3, 28]

The temperature for the hot side for this image is set to 245 °C and for the cold side to 75 °C. With this temperature setting a thermal gradient of 68 °C mm^{-1} is established. The translation velocity is 5 µm s^{-1}.

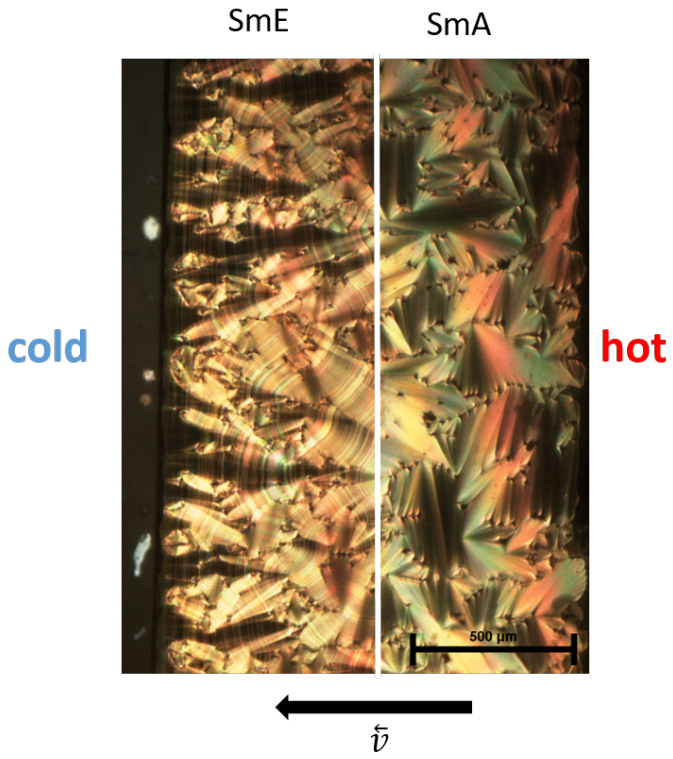

Figure 3.10: POM image during the use of the thermal gradient technique. The arrow indicates the translation direction from hot to cold. The hot side has a temperature of 245 °C and the cold side a temperature of 75 °C. The SmE and the SmA phase are observable.

Figure 3.11 pictures the thermal gradient sample after cooling down to room temperature. Now the sample is in the crystalline phase. The sample is still sandwiched between the two glass plates. The cracks, visible in the image, are due to thermal contraction while cooling down to room temperature. For further investigations the upper glass plate is removed. When separating the two glass plates, the crystal breaks and sticks to both glass substrates. A very inhomogeneous surface is the result (figure 3.12).

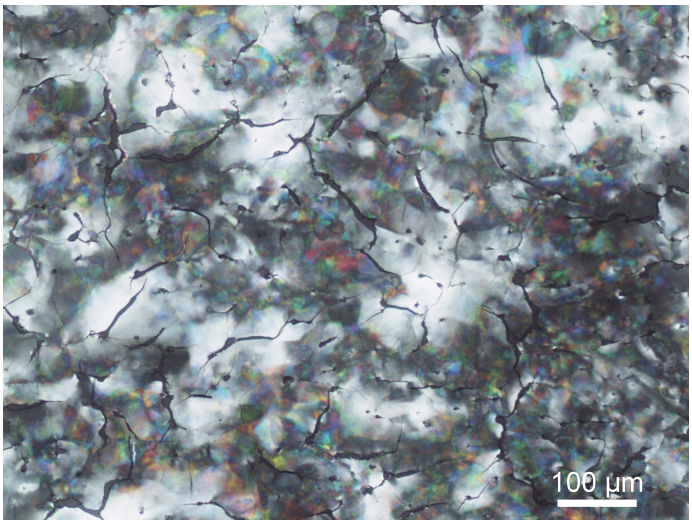

Figure 3.11: POM image after using the thermal gradient technique, cooled down to room temperature and still sandwiched. The cracks come from the thermal contraction while cooling down.

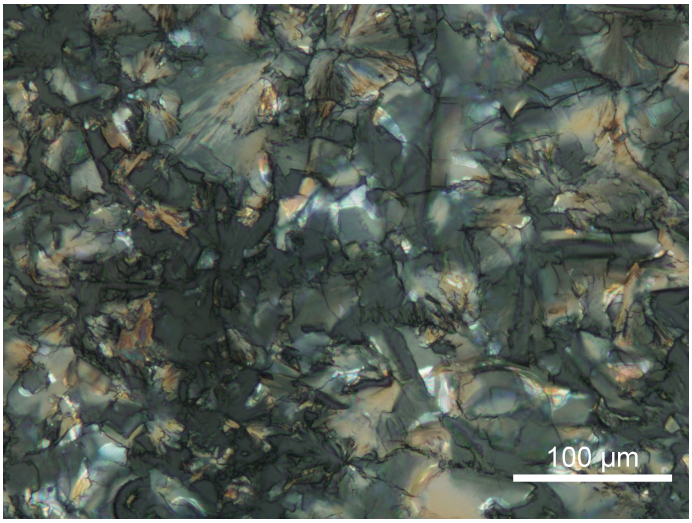

Figure 3.12: POM image at room temperature after using the thermal gradient technique and after separating the two glass substrates. The cracks come from the thermal contraction while cooling down. The crystals between the two glass plates break and both substrates are covered with an inhomogeneous film.

First the samples were investigated by XRD. The resulting XRD curves for all the samples are plotted in figure 3.13. The top curve is depicting the one for the fastest translation velocity and going further down, the translation velocity decreases. The curves are vertically shifted for better comparison. All curves show a comparable behavior and on the first look it seems that the translation velocity does not influence the crystallization. All the samples show the peak positions of the bulk structure. However, a detail to point out is that the peak widths are alternating. The marked peaks are illustrating that the odd peaks are broad whereas the even peaks are quite sharp.

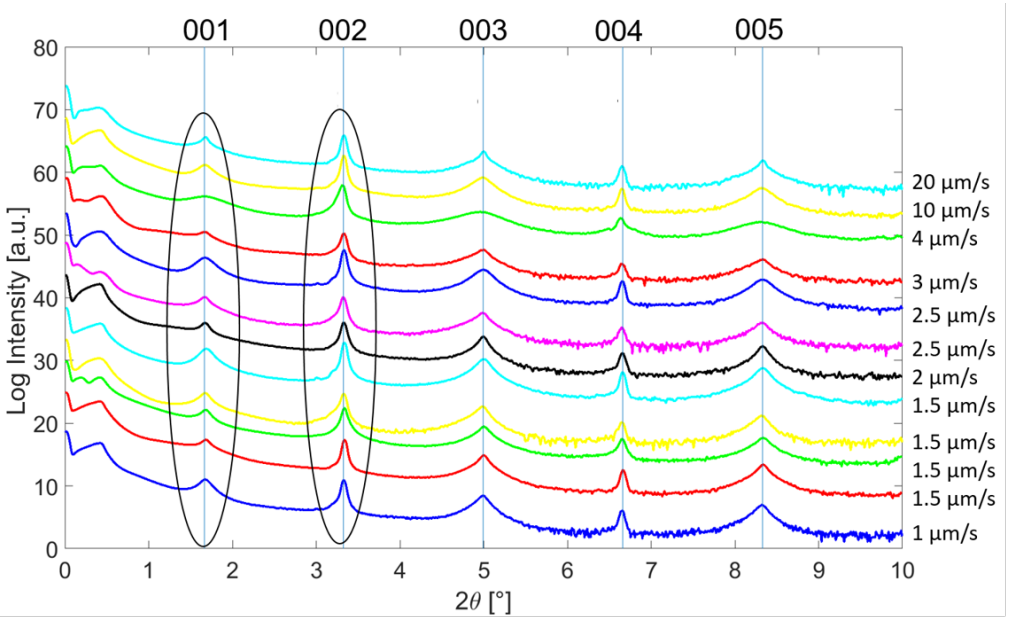

Figure 3.13: The XRD overview of the thermal gradient crystallization samples with the position of the bulk peaks and the translation velocity of the samples. The marked 001 peak is representative for the broad peaks and the 002 for the sharp peaks. All curves were measured from 0° to 30° but for a better presentation the plot just shows the part from 0° to 10° and the curves are vertically shifted.

To have a better comparison between the gradient samples and the drop-casted ones, figure 3.14 shows both curve types in one graph. The blue

one is a gradient sample and the red one is a untreated drop-casted one. As can be seen, the even 00l peak shapes are quite the same for both samples and the odd 00l ones are far broader for the gradient samples than for the drop-casted ones.

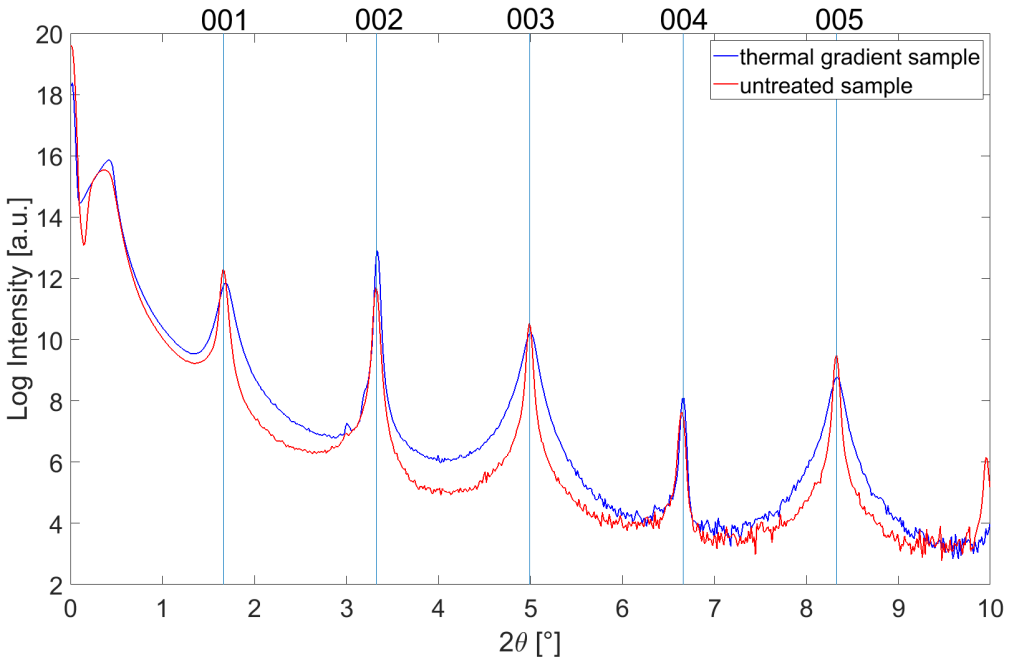

Figure 3.14: Peak broadening. The red curve is the XRD pattern for the drop-casted sample and the blue curve belongs to a thermal gradient sample. The remarkable thing is that the odd 00l peaks of the thermal gradient sample are far broader then the ones for the untreated sample. The even peaks have the same shape for both the samples.

To make it more illustrative the corresponding hkl planes are added to the unit cell. On the left side of figure 3.15 there are the planes that produce the broad peaks and on the right side the planes for the sharp peaks are drawn.

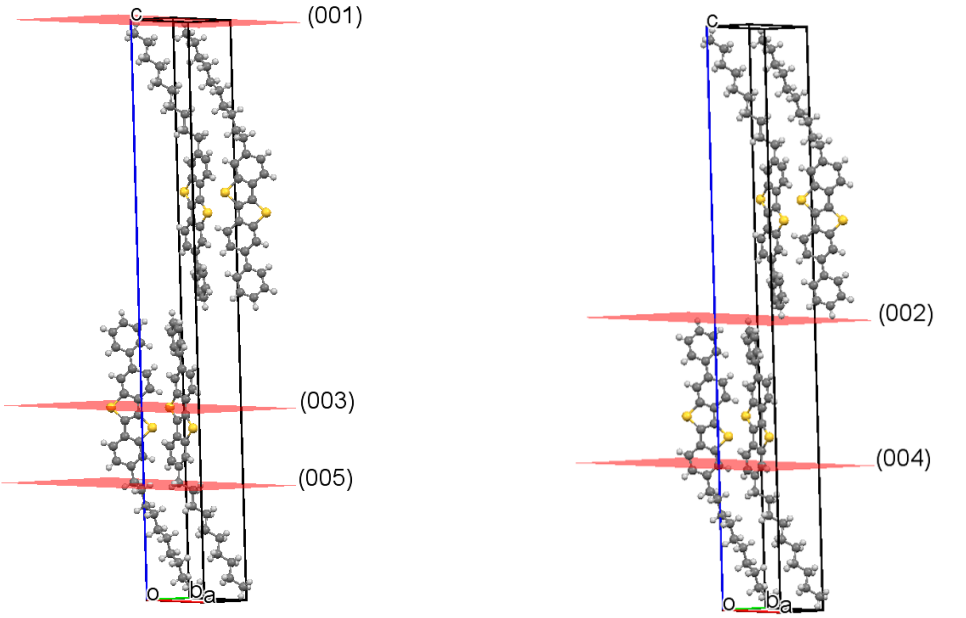

(a) hkl planes that contribute to the broad peaks

(b) hkl planes that contribute to the sharp peaks

Figure 3.15: 00l planes of the bulk structure

To get a closer look, Williamson-Hall plots were created for all the samples. A representative plot is depicted in figure 3.16. The interesting aspect is that not all peaks can be fitted with one linear fit as before but with two and the remarkable thing is that the even peaks lie on one line and the odd peaks on a different one. The corresponding crystallite sizes and micro-strains are calculated, figure 3.18. The calculated crystallite sizes from the even 00l peaks range from 1285 Å to 7709 Å and for the odd 00l peaks the calculated crystallite size is significantly smaller, ranging from 271 Å to 964 Å. So the sharp peaks (even 00l) result from bigger crystallites and the broad ones (odd 00l) from smaller ones. The micro-strain is inversely to the crystallite size; the bigger crystallites have smaller micro-strain. That is the predominantly observed behavior and makes

sense because there is an increase of grain boundaries and dislocations by small crystallites. [29] One sample shows the inversely behavior and there the bigger crystallites have bigger micro-strain, figure 3.17

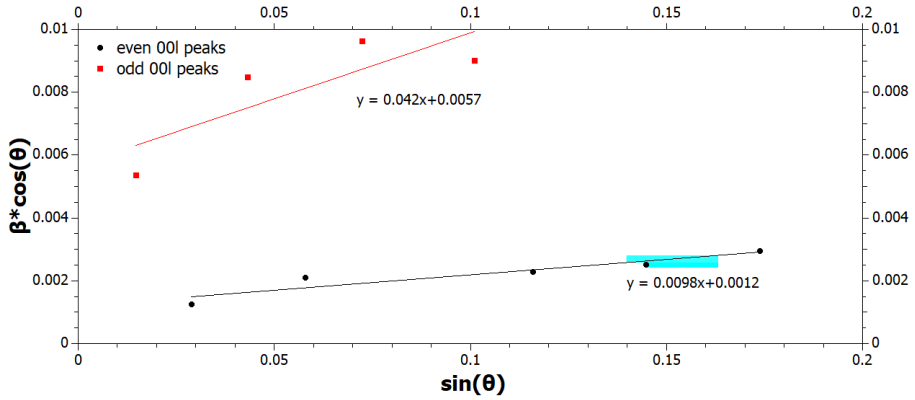

Figure 3.16: Williamson-Hall for a thermal gradient crystallization sample. All data points belong to one XRD pattern of figure 3.13, namely the green curve with $4\,\mu m\,s^{-1}$. The odd 00l (red) and the even 00l peaks (black) can be separated and fitted with different linear functions.

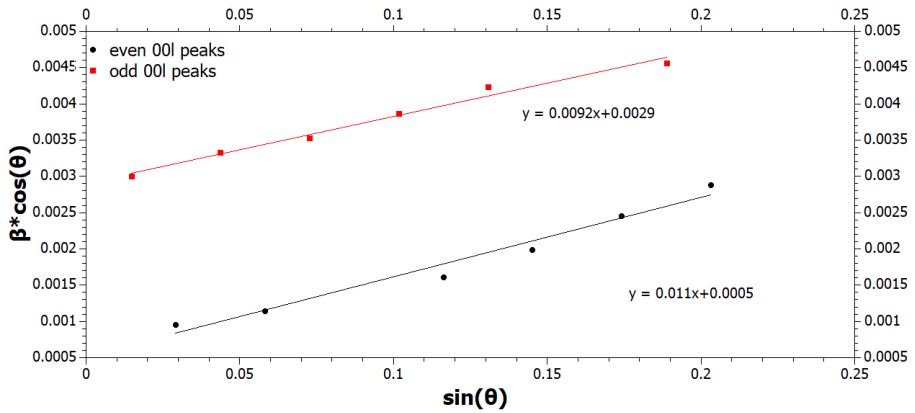

Figure 3.17: Williamson-Hall for a thermal gradient crystallization sample. All data points belong to one XRD pattern of figure 3.13, namely the yellow curve with $1.5\,\mu m\,s^{-1}$. The odd 00l (red) and the even 00l peaks (black) can be separated and fitted with different linear functions.

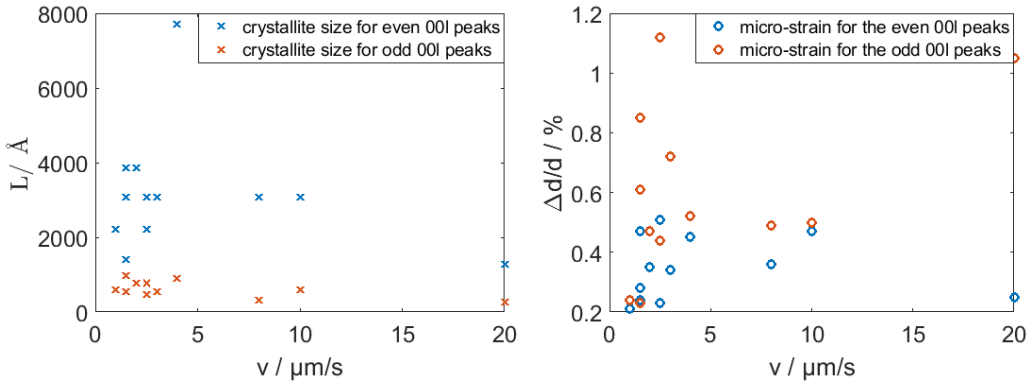

(a) Crystallite size (L) over velocity (v) (b) Micro-strain ($\Delta d/d$) over velocity (v)

Figure 3.18: Williamson Hall evaluation. The even peaks result from bigger crystallites than the odd peaks (a). For the smaller crystallites the micro-strain is bigger than for the bigger crystallites (b). However, there is one deviation from this trend in the low velocity range.

A closer look at figure 3.18 shows that for smaller translation velocities bigger crystallites are observed. For $20\,\mu m\,s^{-1}$ the crystallite sizes are smaller than for the slower translated samples. The broadness is dependent on the translation velocity through the gradient, as can be seen in figure 3.19. The faster the sample translates through the gradient the broader the odd peaks.

So what is causing the different peak widths. According to the Scherrer formula the peak width should follow a continuous increase. So the first approach is that there is a mixture of phases present induced by recrystallizing from the melt and the peaks of the phases overlap to one peak. If there are more phases present, it should be visible in a GIXD measurement.

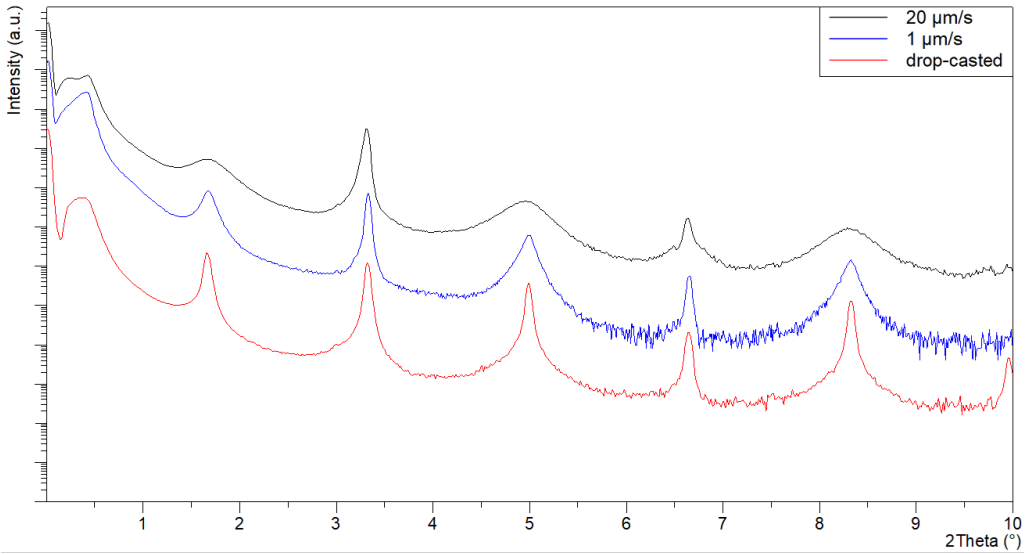

Figure 3.19: Peak broadening. The drop-casted sample shows peaks with almost the same peak widths. The thermal gradient crystallization samples show higher peak broadening for the odd 00l peaks the higher the translation velocity is.

The GIXD map of a thermal gradient crystallization sample is shown in figure 3.20. The black stars correspond to the calculated positions for the diffraction pattern of the bulk phase. As can be seen the positions fit quite well. The white circles are proportional to the calculated intensity for each peak. The bright yellow spots in the map are the measured intensities of the film. The calculated and measured intensities fit quite well. The rings in the GIXD map show Debye-Scherrer cones for the 110, 020 and 120 Bragg reflections. These correspond to the herringbone structure, so the bulk phase is clearly present. [30] No other phase can be identified via GIXD so the peak broadening cannot come from a different phase and must have some other reason.

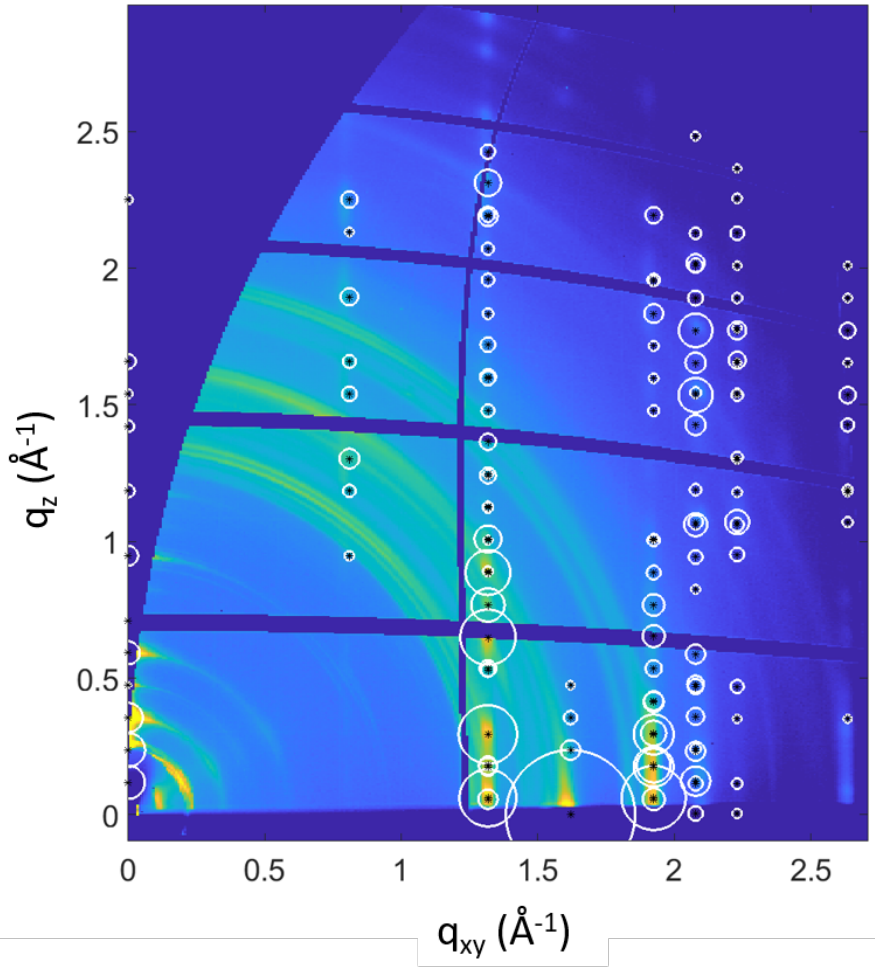

Figure 3.20: The GIXD map of a thermal gradient crystallization sample. The parameters for the sample preparation are 65 µl of a 8 mg/ml solution drop-casted, thermal gradient 245 °C to 65 °C and translation velocity 1.5 µm s^{-1}

3.3 Heating / cooling experiments

3.3.1 Heating of thermal gradient crystallization sample

One of the thermal gradient crystallized samples was heated up and in-situ XRD measurements were done at several temperatures. The DHS 900 mounted on the Panalytical was used for that. The temperatures were set manually. Figure 3.21 plots temperature over 2θ.

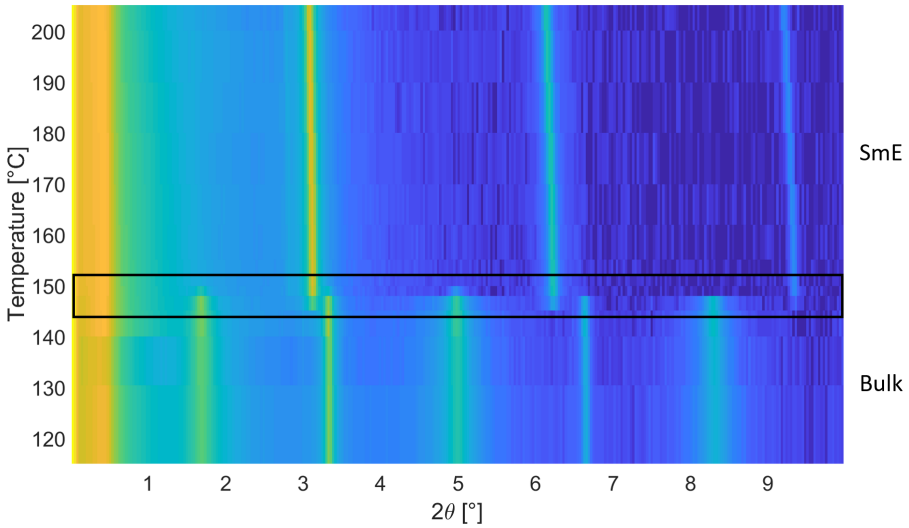

Figure 3.21: 2D surface plot. Yellow corresponds to high intensity and blue to low intensity. The change of the Bragg peak positions over the temperature is observable. The black box is the area where the phase transition happens and the XRD pattern are shown in figure 3.22.

The measured intensity is color coded. Yellow indicates high intensity, so from 115 °C to 140 °C the bulk peaks are present. There is a slight shift of the bulk peaks to smaller angles that indicates a higher d-spacing due to thermal expansion. Between 145 °C and 148 °C both the bulk phase and the SmE phase is present (figure 3.22). Above 150 °C the SmE phase is visible up to 215 °C. In figure 3.22 a closer look at the phase transition

is depicted. The arrows point out that at 145 °C (green curve) both, the crystal and the SmE, phases are present and at 148 °C (orange curve) the intensity of the bulk peaks decrease and the SmE peaks get stronger. At 150 °C (red curve) the bulk peaks are gone, so the transition to the SmE phase is completed.

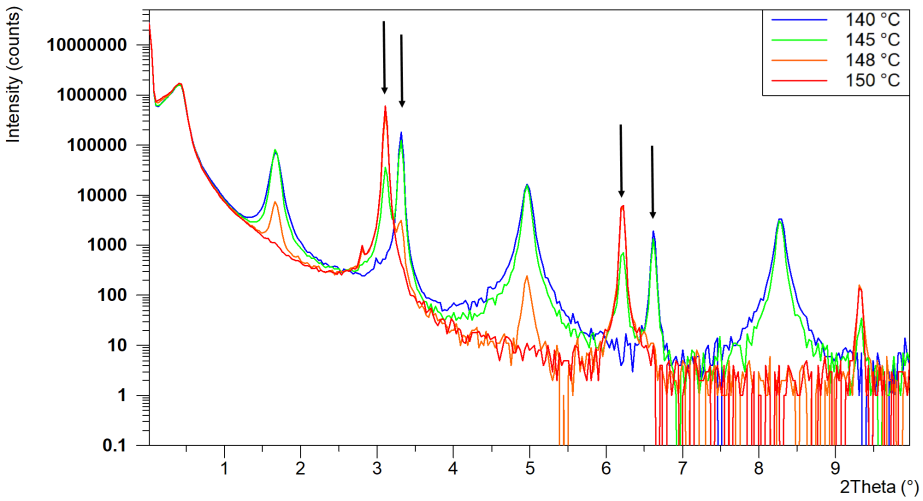

Figure 3.22: A closer look at the crystal to SmE phase transition. The arrows mark the presence of the crystal and the SmE phase in the green curve.

From the peak positions the d-spacing can be calculated with Bragg's law. In figure 3.23 the d-spacing trend over the temperature is shown. The bulk phase has a d/2-spacing of 26.2 Å up to 26.5 Å. That suits the 26.5 Å of half a unit cell quite well. The SmE phase has a d-spacing of 28.4 Å up to 28.9 Å, this is a little bit larger than one upright standing molecule. At 220 °C a back shift to 28.4 Å happens at the SmE to SmA phase transition. The DSC predicts lower transition temperatures as observed. A reason for that is the set-up of the experiment. It takes some time that the sample adjusts to the temperature of the heating stage. Therefore, there can be slight discrepancies between the DSC and the experiment. However, the observed transition temperatures of 148 °C and 220 °C are quite close to the predicted ones of 143 °C and 210 °C.

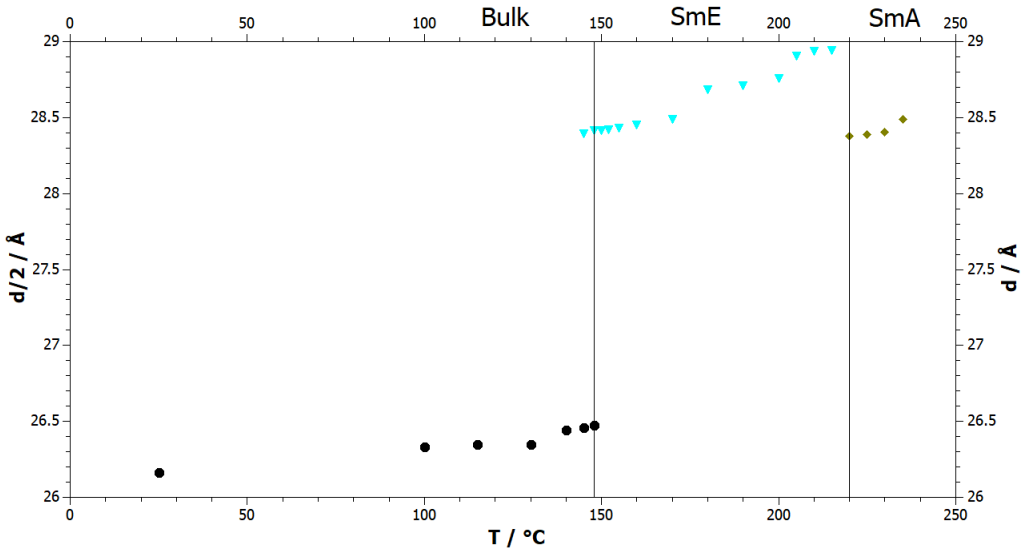

Figure 3.23: The d-spacing over temperature. The different phases can be seen. The left axis is for the bulk phase and the right axes for the SmE and SmA phase.

From this series of XRD measurements, Williamson-Hall plots are created for every single temperature. In figure 3.24 the Williamson-Hall plots for 25 °C, 140 °C and 145 °C (transition to SmE) are shown. The plot shows that the odd and even 00l peaks can be separated until close to the phase transition, then all peaks lie on one line again (145 °C). The Williamson-Hall plot for the SmE phase at 155 °C and the crystal phase at 145 °C is in figure 3.25. As can be seen the SmE line is beneath the crystal line from that results a slightly bigger crystallite size for the SmE phase than for the crystallite size at the phase transition. In figure 3.26 (a) the trend of the crystallite size over the temperature is depicted. In the SmE phase a crystallite size of 1200 Å is established. In figure 3.26 (b) the corresponding micro-strain is plotted. As before the micro-strain is smaller for bigger crystallites and vice versa. In the SmE phase there is not really a trend for the micro-strain observable, only that the micro-strain is smaller than for the crystalline phase.

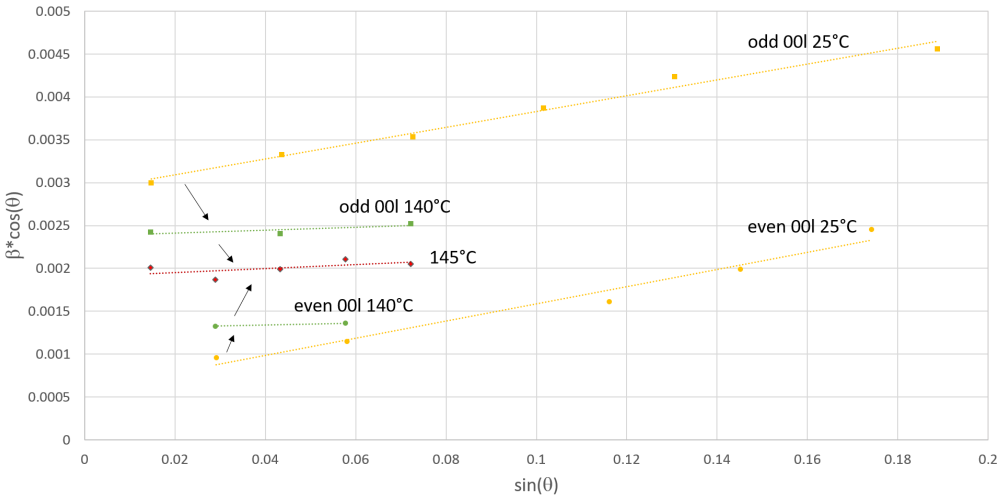

Figure 3.24: Williamson Hall plots for different temperatures.

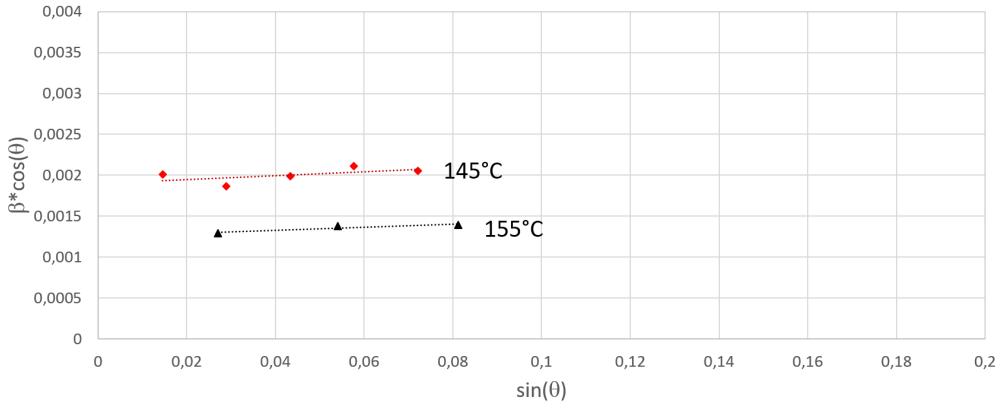

Figure 3.25: Williamson Hall plots close to the phase transition from crystal to SmE. The SmE line is slightly beneath the crystal line. The SmE crystallite size is higher than for the crystal close to the phase transition.

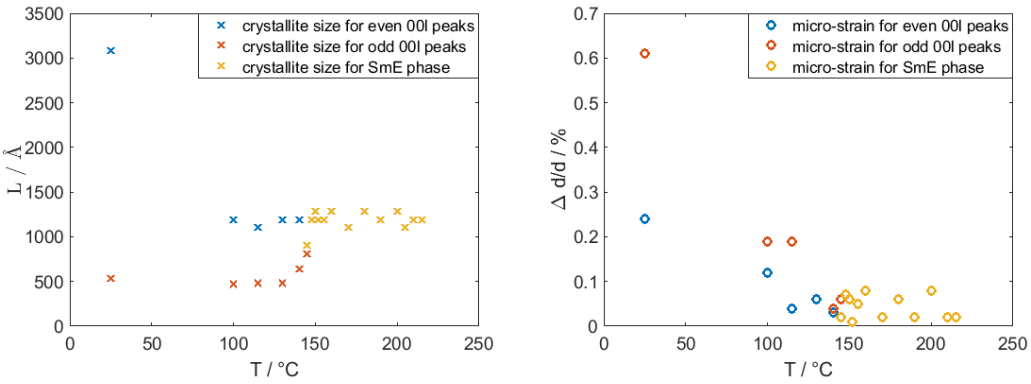

(a) Crystallite size (L) over temperature (T)

(b) Micro-strain over temperature

Figure 3.26: Williamson Hall evaluation

3.3.2 Cooling rate experiment on drop-casted samples

The cooling experiment with different cooling rates is shown in figure 3.27. The XRD patterns and the bulk Bragg peaks are plotted together. Every pattern comes from a different cooling rate. The fast cooling rates, the ones above $10\,^{\circ}\,\mathrm{min}^{-1}$, show a peak shift of the even 00l peaks and low intensity for the odd 00l peaks. The explanation for that is that due to the fast cooling rate the molecules do not have time to move in the perfect crystal position and get stuck in a quite unordered structure with a slightly bigger d-spacing as the bulk structure. For lower cooling rates the same behavior as for the thermal gradient samples is observed. Broad and sharp peaks are alternating. For very low cooling rates the behavior is not completely understood.

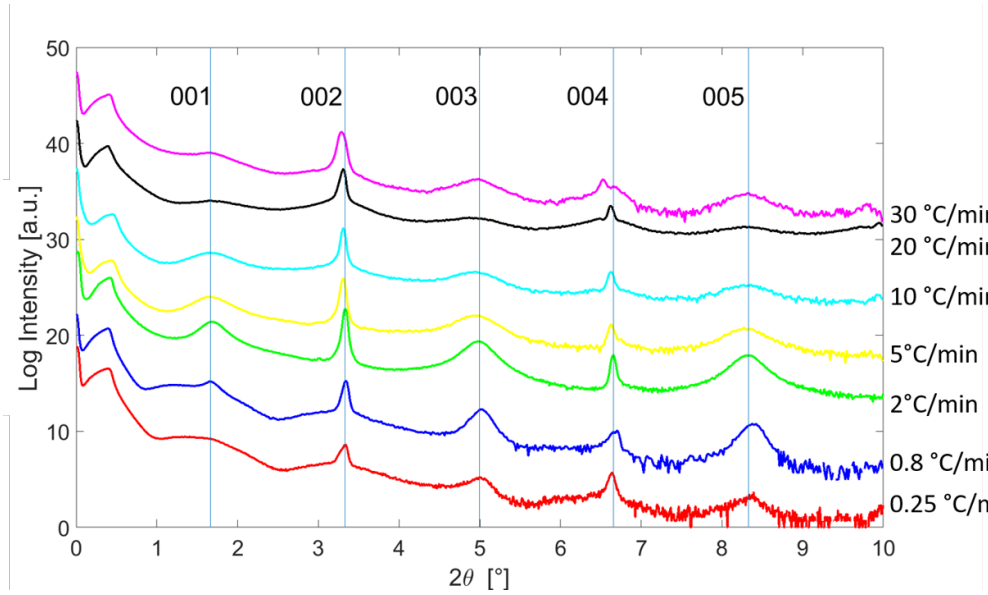

Figure 3.27: The XRD overview of the cooling series with the cooling rate.

A GIXD measurement was performed for the sample with a cooling rate of $5\,^{\circ}\mathrm{C\,min^{-1}}$. The GIXD map (figure 3.28) again shows the bulk structure. The white circles indicate again the calculated intensity, the larger the circle the higher the intensity. The big white circles are located at spots with high measured intensity, so the bulk structure fits very well.

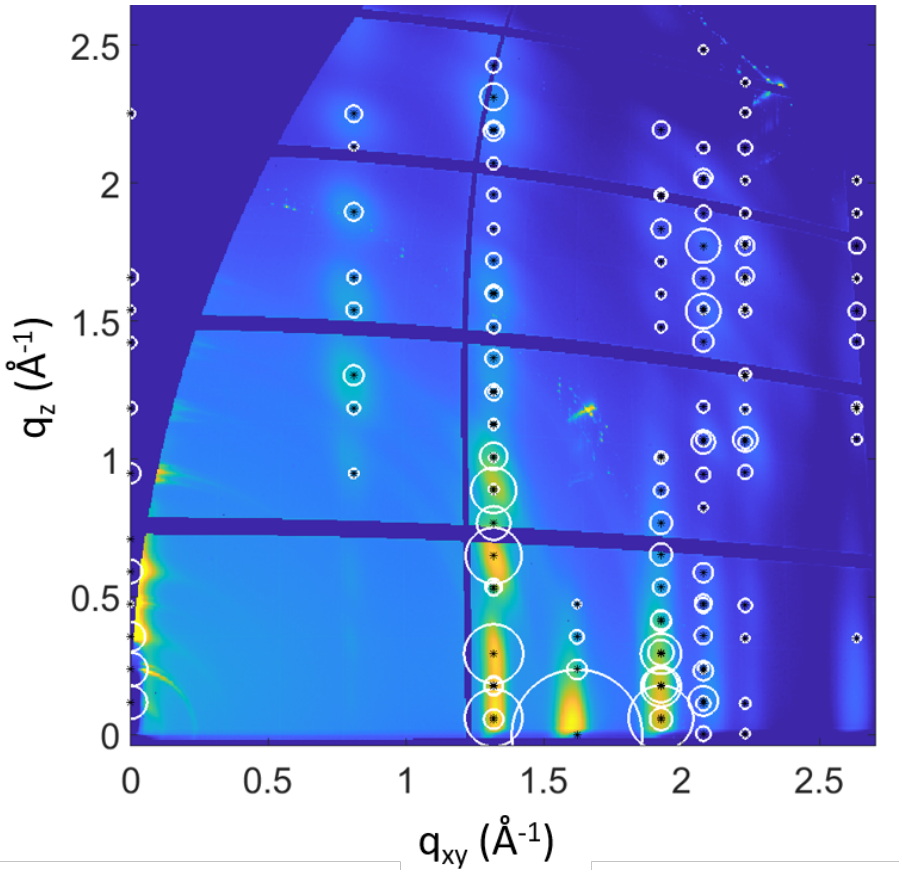

Figure 3.28: The GIXD pattern of the sample with the 5 °C min^{-1} cooling rate.

4 Conclusion

4.1 Comparison of two material sources

The comparison of the two material sources shows that there is no significant difference between the Milano and Brussels material. The XRF analysis shows just a slight difference in the impurities, but over all both compounds are very clean. The film formation, crystal structure and thermal behavior are comparable. Both materials show plate like crystallites in different sizes. The crystal structure is assigned to the known bulk structure and the predicted phase transitions are observable for both materials.

4.2 Thermal gradient crystallization samples

During the thermal gradient crystallization method the phase transition from SmA to SmE is observable with the polarized optical microscope. After cooling down to room temperature the crystal phase is present. The X-ray diffraction measurements show a preferred out-of-plane orientation of the 00l planes. That corresponds to two upright standing molecules on top of each other and can be assigned to the known bulk structure. However, alternating peak widths appear. The odd 00l peaks are broad and the even 00l peaks are narrow. A Williamson-Hall analysis shows that the two peak series result from different crystallite sizes. The sharp peaks result from crystallites of a size ranging from 130 nm to 770 nm

and the broad ones from crystallite sizes ranging from 30 nm to 100 nm. The micro-strain is inversely to the crystallite size; smaller crystallites exhibit larger micro-strain. That is the expected behavior due to the increase of grain boundaries and dislocations by small crystallites. The peak positions of the grazing incidence X-ray diffraction measurements are perfectly matching the known crystal structure and also the intensities are comparable. This observation confirms that there is only one phase present in the samples. In addition to that, all the peaks melt at the expected same temperature. However, the recrystallization process induces a molecular disorder in the crystal. Heating the gradient crystallization samples leads to a healing of the defects. Close to the SmE phase transition temperature a Williamson Hall evaluation of the X-ray diffraction measurement shows a merge of the odd and even peaks to one line and an approximate crystallite size of 120 nm .

4.3 Heating / cooling experiments

The influence of the cooling rate on the crystallization behavior was checked by a cooling series with different cooling rates. In general the same behavior as for the gradient crystallization samples is observed. Broad and narrow peaks alternate. However, the cooling rate influences the broadness of the odd 00l peaks. The higher the cooling rate the broader the peaks. Due to the high cooling rate the molecules get stuck in a disorderd crystal structure. However, the over all crystal structure is still the known bulk phase. The gradient crystallization method produces better aligned crystals than just cooling down the melt as a whole, but a certain disorder is present in both cases.

Bibliography

[1] Mahmut Kus et al. "Chapter 24 - Synthesis of Nanoparticles." In: *Handbook of Nanomaterials for Industrial Applications*. Ed. by Chaudhery Mustansar Hussain. Micro and Nano Technologies. Elsevier, 2018, pp. 392–429. ISBN: 978-0-12-813351-4. URL: http://www.sciencedirect.com/science/article/pii/B9780128133514000250 (cit. on p. 1).

[2] Hideaki Ebata et al. "Highly Soluble [1]Benzothieno[3,2-b]benzothiophene (BTBT) Derivatives for High-Performance, Solution-Processed Organic Field-Effect Transistors." In: *Journal of the American Chemical Society* 129.51 (2007). PMID: 18044892, pp. 15732–15733. DOI: 10.1021/ja074841i. eprint: https://doi.org/10.1021/ja074841i. URL: https://doi.org/10.1021/ja074841i (cit. on p. 1).

[3] Hiroaki Iino, Takayuki Usui, and Jun-Ichi Hanna. "Liquid crystals for organic thin-film transistors." In: *Nature communications* 6 (Apr. 2015), p. 6828. DOI: 10.1038/ncomms7828 (cit. on pp. 1–3, 35).

[4] Hiromi Minemawari et al. "Crystal structure of asymmetric organic semiconductor 7-decyl-2-phenyl[1]benzothieno[3,2-b][1]benzothiophene." In: *Applied Physics Express* 7.9 (Sept. 2014), p. 091601. DOI: 10.7567/apex.7.091601. URL: https://doi.org/10.7567%2Fapex.7.091601 (cit. on p. 2).

[5] Kazuo Takimiya et al. "Organic Semiconductors Based on [1]Benzothieno[3,2-b][1]benzothiophene Substructure." In: *Accounts of Chemical Research* 47.5 (2014). PMID: 24785263, pp. 1493–1502. DOI: 10.1021/ar400282g. eprint: https://doi.org/10.1021/ar400282g. URL: https://doi.org/10.1021/ar400282g (cit. on p. 3).

[6] G. Höhne, W.F. Hemminger, and H.J. Flammersheim. *Differential Scanning Calorimetry*. Springer Berlin Heidelberg, 2013. ISBN: 9783662067109 (cit. on p. 3).

[7] Alexandre C. Dimian, Costin S. Bildea, and Anton A. Kiss. "Chapter 11 - Batch Processes." In: *Integrated Design and Simulation of Chemical Processes*. Ed. by Alexandre C. Dimian, Costin S. Bildea, and Anton A. Kiss. Vol. 35. Computer Aided Chemical Engineering. Elsevier, 2014, pp. 449–488. DOI: https://doi.org/10.1016/B978-0-444-62700-1.00011-5. URL: http://www.sciencedirect.com/science/article/pii/B9780444627001000115 (cit. on p. 4).

[8] Michael F. Ashby and David R.H. Jones. "Chapter 8 - Kinetics 2—Nucleation." In: *Engineering Materials 2 (Fourth Edition)*. Ed. by Michael F. Ashby and David R.H. Jones. Fourth Edition. International Series on Materials Science and Technology. Boston: Butterworth-Heinemann, 2013, pp. 141–154. DOI: https://doi.org/10.1016/B978-0-08-096668-7.00008-5. URL: http://www.sciencedirect.com/science/article/pii/B9780080966687000085 (cit. on pp. 4–6).

[9] K.T. Wilke and J. Bohm. *Kristallzüchtung*. Kristallzüchtung Bd. 1. Deutscher Verlag der Wissenschaften, 1973 (cit. on pp. 9, 10).

[10] Robin P. Mooney et al. "An experimental–numerical method for estimating heat transfer in a Bridgman furnace." In: *Applied Thermal Engineering* 67.1 (2014), pp. 61–71. ISSN: 1359-4311. DOI: https://doi.org/10.1016/j.applthermaleng.2014.02.048. URL: http://www.sciencedirect.com/science/article/pii/S1359431114001409 (cit. on p. 9).

[11] Guillaume Schweicher et al. "Toward Single Crystal Thin Films of Terthiophene by Directional Crystallization Using a Thermal Gradient." In: *Crystal Growth & Design* 11.8 (2011), pp. 3663–3672. DOI: 10.1021/cg2007793. eprint: https://doi.org/10.1021/cg2007793. URL: https://doi.org/10.1021/cg2007793 (cit. on pp. 10, 14).

[12] Priyanka Kajal, Kunal Ghosh, and Satvasheel Powar. "Manufacturing Techniques of Perovskite Solar Cells." In: Jan. 2018, pp. 341–364. ISBN: 978-981-10-7205-5. DOI: 10.1007/978-981-10-7206-2_16 (cit. on p. 11).

[13] Bernhard Wedl et al. "Crystallisation kinetics in thin films of dihexyl-terthiophene: the appearance of polymorphic phases." In: *RSC Adv.* 2 (10 2012), pp. 4404–4414. DOI: 10.1039/C2RA20272G. URL: http://dx.doi.org/10.1039/C2RA20272G (cit. on p. 11).

[14] W. Demtröder. *Experimentalphysik 2, Elektrizität und Optik*. 7. Auflage. Experimentalphysik / Wolfgang Demtröder. Springer Berlin Heidelberg, 2017. ISBN: 9783662557907 (cit. on p. 16).

[15] Joshua Lin (https://physics.stackexchange.com/users/60080/joshua-lin). *Do electromagnetic waves occupy varying amounts of space, or do they simply vary in magnitude?* Physics Stack Exchange. eprint: https://physics.stackexchange.com/q/171144. URL: https://physics.stackexchange.com/q/171144 (cit. on p. 16).

[16] Guillaume Schweicher. *Alignment of organic semicondutors in a thermal gradient*. Université libre de Bruxelles, Brussels, Belgium. 2012 (cit. on pp. 16, 17).

[17] https://wpo-altertechnology.com/xrf-x-ray-fluorescence-spectroscopy-hi-rel-parts/ (cit. on p. 18).

[18] D. Schwarzenbach. *Crystallography*. John Wiley, 1996. ISBN: 9780471955986. URL: https://books.google.at/books?id=FyFDAQAAIAAJ (cit. on p. 19).

[19] W. R. Bodlos. *Surface Crystallization Studies of Decyl-Phenyl-Benzothieno-Benzothiophene*. Graz University of Technology. 2018 (cit. on p. 20).

[20] J. Epp. "4 - X-ray diffraction (XRD) techniques for materials characterization." In: *Materials Characterization Using Nondestructive Evaluation (NDE) Methods*. Ed. by Gerhard Hübschen et al. Woodhead Publishing, 2016, pp. 81–124. ISBN: 978-0-08-100040-3. DOI: https://doi.org/10.1016/B978-0-08-100040-3.00004-3. URL: http://www.sciencedirect.com/science/article/pii/B9780081000403000043 (cit. on p. 20).

[21] Zhenan Bao and Jason Locklin. *Organic Field-Effect Transistors*. 1st. Boca Raton, FL, USA: CRC Press, Inc., 2007 (cit. on p. 22).

[22] Benedikt Schrode et al. "GIDVis: a comprehensive software tool for geometry-independent grazing-incidence X-ray diffraction data analysis and pole-figure calculations." In: *Journal of Applied Crystallography* 52.3 (June 2019), pp. 683–689. DOI: 10.1107/S1600576719004485. URL: https://doi.org/10.1107/S1600576719004485 (cit. on p. 23).

[23] A. Khorsand Zak et al. "X-ray analysis of ZnO nanoparticles by Williamson–Hall and size–strain plot methods." In: *Solid State Sciences* 13.1 (2011), pp. 251–256. ISSN: 1293-2558. DOI: https://doi.org/10.1016/j.solidstatesciences.2010.11.024. URL: http://www.sciencedirect.com/science/article/pii/S1293255810004607 (cit. on pp. 23, 24).

[24] P Scherrer. "Bestimmung der Grösse und der inneren Struktur von Kolloidteilchen mittels Röntgenstrahlen [Determination of the size and internal structure of colloidal particles using X-rays]." In: *Nachr. Ges. Wiss. Göttingen* 2 (1918), pp. 98–100 (cit. on p. 24).

[25] University of London Birkbeck College. *Advanced Certificate in Powder Diffraction on the Web*. URL: http://pd.chem.ucl.ac.uk/pdnn/peaks/sizedet.htm (cit. on p. 24).

[26] R. Resel et al. "A heating stage up to 1173K for X-ray diffraction studies in the whole orientation space." In: *Journal of Applied Crystallography* 36.1 (Feb. 2003), pp. 80–85. DOI: 10.1107/S0021889802019568. URL: https://doi.org/10.1107/S0021889802019568 (cit. on p. 25).

[27] Anton Paar GmbH. "DHS1100: a new high-temperature attachment for materials science in the whole orientation space." In: *Journal of Applied Crystallography* 40.1 (Feb. 2007), p. 202. DOI: 10.1107/S0021889806047224. URL: https://doi.org/10.1107/S0021889806047224 (cit. on p. 25).

[28] Lopamudra Chakraborty et al. "Synthesis, mesomorphic and photophysical properties of few d-and f-block metals coordinated to polar Schiff's bases Synthesis, mesomorphic and photo-physical properties of few d-and f-block metals coordinated to polar Schiff's bases." In: *Liquid Crystals* 39 (Apr. 2012), pp. 655–668. DOI: 10.1080/02678292.2012.669854 (cit. on p. 35).

[29] K. Venkateswarlu et al. "Estimation of Crystallite Size, Lattice Strain and Dislocation Density of Nanocrystalline Carbonate Substituted Hydroxyapatite by X-ray Peak Variance Analysis." In: *Procedia Materials Science* 5 (2014), pp. 212–221 (cit. on p. 41).

[30] Gabin Gbabode et al. "X-ray Structural Investigation of Nonsymmetrically and Symmetrically Alkylated [1]Benzothieno[3,2-b]benzothiophene Derivatives in Bulk and Thin Films." In: *ACS Applied Materials & Interfaces* 6.16 (2014). PMID: 25083814, pp. 13413–13421. DOI: 10.1021/am5015315. eprint: https://doi.org/10.1021/am5015315. URL: https://doi.org/10.1021/am5015315 (cit. on p. 43).